Exploring the Potential of Thermal Point Clouds to Assess Crop Water Stress Within Precision Viticulture

Final Thesis Report
May, 2023

Author: Thomas Buunk

Student number: 4422732

Supervisors:

Sergio Vélez Martín

Mar Ariza Sentís

Responsible Professor:

Ron van Lammeren

Preface

This thesis, titled ‘Exploring the Potential of Thermal Point Clouds to Assess Crop Water Stress Within Precision Viticulture’ was written as part of my Master’s program in Geographical Information Management and Applications.

I would like to express my gratitude to my supervisors, Sergio Vélez Martín and Mar Ariza Sentís, whose support and guidance were essential in the completion of this thesis. This thesis would not have been possible without all the data they extensively collected and provided to me. Furthermore, I am thankful for their guidance throughout the research process. They directed me in the right direction and were patient enough to address all my questions during challenging moments.

Abstract

The Crop Water Stress Index (CWSI) has emerged as a valuable tool in Precision Viticulture (PV) for assessing crop water stress over vast areas. This is particularly significant considering the increasing demand for water and limited water resources. Maximizing water efficiency and crop yield through irrigation scheduling is therefore of utmost importance. While various techniques have been employed to improve crop water stress analysis, the use of thermal point clouds remain relatively unexplored. This thesis aims to enhance crop water stress analysis methodologies within PV through the integration of remote sensing, thermal imaging, and point cloud technologies. The study focuses on evaluating the viability of using thermal point clouds to generate 3D point clouds with CWSI values and 2D CWSI orthomosaics. Comparative analysis of these data models determines the appropriateness of employing thermal point clouds for CWSI calculation within PV. Additionally, the research explores the influence of different flight configurations (nadir, oblique, and their combination) on CWSI outcomes, seeking to identify the most effective workflow for CWSI calculation using point clouds. The findings exhibit promising potential, showing that thermal point clouds can be effectively employed to generate CWSI point clouds. The research findings indicate that point clouds offer a more comprehensive representation of the canopy compared to orthomosaics, thus providing more detailed information. Volume calculations show that the combined workflow yields the most accurate results in terms of geometric representation ($R^2 = 0.72$), followed by the nadir flight ($R^2 = 0.68$), and finally the oblique flight ($R^2 = 0.54$). This outcome indicates that the combined workflow is the optimal approach for CWSI calculations utilizing point clouds.

Keywords: Crop Water Stress Index, 3D Thermal Point Clouds, UAV Remote Sensing, Thermal Imaging, Precision Viticulture.

Contents

List of figures

List of tables

List of abbreviations

2D	Two-dimensional
3D	Three-dimensional
CHM	Canopy Height Model
CWSI	Crop Water Stress Index
CWSIe	Empirical Crop Water Stress Index
CWSIs	Statistical Crop Water Stress Index
CWSIt	Theoretical Crop Water Stress Index
DSM	Digital Surface Model
DTM	Digital Terrain Model
EM	Electromagnetic
GCP	Ground Control Point
IR	Infrared
LAI	Leaf Area Index
LiDAR	Light Detecting and Ranging Systems
NDVI	Normalized Difference Vegetation Index
NIR	Near-infrared
PA	Precision Agriculture
PV	Precision Viticulture
RGB	Red, green, blue
ROI	Region of interest
SfM	Structure from Motion
SWIR	Shortwave infrared
TIR	Thermal infrared
UAV	Unmanned Aerial Vehicle
VI	Vegetation Index
VIS	Visible
VPD	Vapor pressure deficit

1. Introduction

1.1 Context

Precision Agriculture (PA) is an innovative and effective approach to improve crop performance, rise economic benefits and mitigate the environmental impact by enhancing crop-managing practices and limiting the use of pollutants (Comba et al., 2019). PA achieves these goals by using a range of advances technologies and cost-effective solutions that manage the temporal and spatial variability related to agriculture (Sassu et al., 2021). Precision Agriculture techniques have been increasingly implemented in viticulture over the last two decades, resulting in the practice called Precision Viticulture (PV) (Santesteban, 2017).

Accurate crop monitoring procedures are essential for the successful implementation of PV processes. In this regard, remote sensing has emerged as a valuable approach, capable of providing vast amounts of data that provide valuable insights into various aspects of crop health and management (Comba et al., 2019). Remote sensing techniques enable the assessment of spatial patterns in crop biomass and yield through the utilization of diverse vegetation indices in combination with physiological traits. Common applications are Leaf Area Index (LAI) estimation, nutrient deficiency detection and health status for precise pesticide application (Matese & Di Gennaro, 2015)

The introduction of the Unmanned Aerial Vehicle (UAV) has significantly boosted PV, complementing the development of satellite and aircraft remote sensing devices (Sassu et al., 2021). While satellite and aircraft remote sensing devices have improved the spatial and temporal resolution in studying plant features, aircrafts are expensive and the spatial resolution of satellites is insufficient for PV (Sassu et al., 2021). In contrast, UAVs offer a cost-effective solution through the capability to carry sensors that provide high spatial and temporal resolution (Zhang & Kovacs, 2012), making them ideal for practices within PV.

Additionally, PV benefits from the utilization of three-dimensional (3D) point clouds in crop monitoring, beyond the traditional use of two-dimensional (2D) mosaicked imagery from multispectral images (Comba et al., 2019). A point cloud is a large dataset consisting of points that correspond to a geodetic reference frame, representing the reflection of light from visible surfaces of objects (Comba et al., 2019). These point clouds can be created directly from laser scanners, typically through Light Detecting And Ranging Systems (LiDAR) (Mack et al.,

2017). Alternatively, they can be created through multispectral and thermal imagery by software that relies on Structure from Motion (SfM) (Comba et al., 2019). SfM is a photogrammetry technique that creates a 3D structure from multiple 2D images through feature extraction and matching (Schonberger & Frahm, 2016).

Moreover, the application of thermal imaging in the agricultural sector has increased in recent years due to advancements in sensors and reduced costs (Messina & Modica, 2020). Infrared thermal imaging is a non-contact and non-destructive technique that enables temperature mapping of materials, making it especially useful for fields such as agriculture. Thermal imaging has found numerous applications within agriculture, including bruise detection, irrigation scheduling, estimating crop yield and pathogen detection (Vadivambal & Jayas, 2011).

Furthermore, thermal imaging proves to be a reliable method for assessing crop water stress, as changes in plant temperature occur when they experience water deficits. Water deficits in plants induces stomatal closure, leading to a reduction in transpiration rate, reducing the evaporative cooling which in turn increases the leaf temperature (Buckley, 2019). The Crop Water Stress Sndex (CWSI) is an index that is derived from canopy temperature and has been applied to assess water deficit in various crops, including grapevines (Gutiérrez et al., 2018). The CWSI has become a valuable index in PA and PV due to its capability to efficiently assess crop water stress accurately over substantial areas. Due to the growing demand for water across multiple sectors and the negative effects of climate change on water resources, it has become essential to prioritize the efficient utilization of water for crop productivity. The insights provided by CWSI analysis can be applied to optimize irrigation scheduling, thereby maximizing water efficiency and crop yield (Zhou et al., 2021).

While temperature is regarded as a valuable parameter for crop monitoring activities, multisensor approaches are often required to increase accuracy (Narvaez et al., 2017). The fusion of thermal data with 3D data, resulting in thermal point clouds, has become a useful method in multiple disciplines, since it enhances environmental monitoring practices (Jurado et al., 2022). Thermal point clouds have been successfully implemented in environmental endeavours such as the characterization of forest canopies (Webster et al., 2018) and assessing radiation dynamics of soil surfaces (González et al., 2019). However, most studies pertaining

to thermal point clouds have focused on different fields, such as energy inspections in buildings (Jurado et al., 2022).

This study aims to bridge the existing research gap by exploring the utilization of thermal point clouds within the context of PV. Specifically, a crop water stress analysis of a vineyard is conducted using thermal point clouds. By combining the aforementioned benefits of remote sensing, thermal imaging and point clouds, there is the potential to further improve existing methodologies for crop water stress analysis.

1.2 Research objectives

The primary objective of this study is to assess the potential of employing thermal point clouds in the context of precision viticulture. To achieve this, the study involves the generation of both 3D point clouds with CWSI values and 2D CWSI orthomosaics. By calculating and analysing the differences between these two data models, the suitability of using thermal point clouds for CWSI calculation can be determined.

Traditional remote sensing CWSI analysis typically relies on 2D orthomosaics (Bian at al., 2019; Bahat et al., 2021l; Araújo-Paredes et al., 2022), which provide information mainly about the top of the canopy. In contrast, 3D point clouds can offer a more comprehensive representation of the canopy (Weiss & Baret., 2017; Pagliai et al., 2022), providing additional insights into the side of the canopy and its influence on the CWSI calculation. To fully explore the potential of using thermal point clouds for CWSI analysis, the study employs multiple workflows, consisting of a nadir and oblique flight, as well as the combination of the two.

The study aims to investigate whether the flight configuration has an impact on the CWSI result and, if so, determine which workflow is most effective for CWSI calculation using point clouds. By examining the influence of flight configurations on CWSI outcomes and comparing the accuracy of different workflows, valuable insights can be gained to optimize the utilization of thermal point clouds in CWSI analysis within precision viticulture.

1.3 Research questions

Based on the objectives of this research, the following research question has been developed:

- *To what extent can thermal point clouds be utilised to assess water stress in precision viticulture?*

To address this research question, the study is subdivided into the following sub-questions:

- RQ1 - What is the current state of water stress studies using multispectral and thermal UAV imagery data?

- RQ2 - How can thermal UAV data effectively be utilized to generate CWSI orthomosaics and CWSI point clouds?

- RQ3 - What are the differences between the data models?

- RQ4 – What is the influence of the flight angle on the CWSI calculation?

2. Theoretical Framework

2.1 Thermal Imaging

Temperature measurement methods used to rely on traditional instruments such as thermometers and thermocouples, which require direct contact with the material and provide localized temperature readings. However, the advent of infrared thermal imaging using remote sensors has revolutionized temperature measurement capabilities (Vadivambal & Jayas, 2011). This non-contact and non-invasive technique enables the mapping of large areas in a single scan, expanding the possibilities for temperature analysis.

Infrared thermal imaging is based on the principle that all objects above -273 °C (0 K) emit radiation, and this emitted radiation is directly related to their temperature (Khanal et al., 2017). By capturing this radiation using thermal sensors, the information can be converted into temperature values. To understand the specific range in which thermal radiation is emitted and detected, **Figure 1** provides an overview of the electromagnetic (EM) spectrum, highlighting the infrared (IR) region. The IR region can be categorized into two distinct regions: the reflected-IR region (0.7-3.0 µm), depicted in grey, and the emitted-IR region (3.0-100 µm), depicted in red. Within the emitted-IR region, there are three subcategories: the mid-wave infrared (MWIR) range (3-8 µm), the long-wave infrared (LWIR) range (8-15 µm), and the far infrared (FIR) range (15-100 µm).

In the context of thermal remote sensing for vegetation studies, the thermal infrared (TIR) spectral range is of particular interest. While the exact definition of the TIR range may vary across different fields and applications, the widely accepted range for TIR remote sensing in vegetation studies is typically considered to be 3-14 µm, which encompasses the MWIR and LWIR ranges (Neinavaz et al., 2021). **Figure 1** depicts the TIR range at the bottom. The LWIR part of the TIR range is particularly relevant for thermal remote sensing as it captures the emitted radiation from landscape features such as soil, water, and vegetation (Messina & Modica, 2020).

.

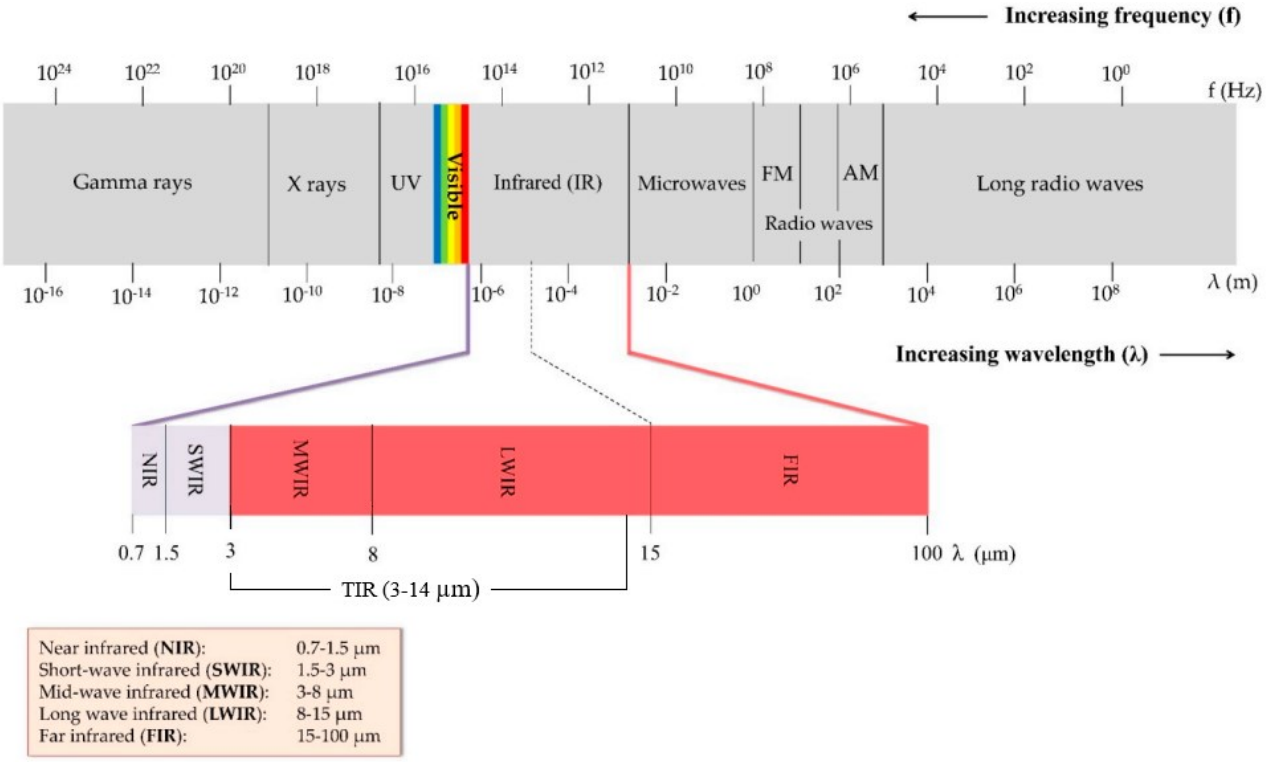

Figure 1: Electromagnetic spectrum, highlighting the IR range (grey and red) and the TIR range in the bottom. Source: Messina & Modica (2020), edited by author.

Besides thermal imaging, sensors that operate in the visible (VIS), near-infrared (NIR) and Shortwave infrared (SWIR) part of the spectrum are also useful for agricultural applications (Wójtowicz et al., 2016). By combining two or more bands in these wavelengths, numerous vegetation indices (VIs) have been established, enabling the estimation of various plant characteristics such as biomass, leaf area, ground cover and chlorophyll content (Khanal et al., 2017). Among these indices, the Normalized Difference Vegetation Index (NDVI), proposed by Rouse et al. (1974), is widely used. The index is calculated by dividing the difference in reflectance between the NIR and red regions by the sum of these two regions. Vegetation indices, such as the NDVI, are primarily derived from the spectral reflectance of vegetation pigments, particularly chlorophyll content (Zhang et al., 2021). In contrast, thermal imaging relies on the measurement of the surface temperature of plants, which is more sensitive to changes or damage in crop growth and can therefore sometimes respond faster than vegetation indices (Khanal et al., 2017)

Due to its ability to detect changes at an early stage, recent technological developments and the reduction of sensor costs, thermal imaging has experienced a surge of popularity within the

field of PA (Khanal et al., 2017). Thermal imaging can be applied to numerous aspects of monitoring in agriculture. The most common applications include monitoring crop water stress for irrigation scheduling, determining disease and pathogen-infected crops, mapping crop yield, mapping soil texture, and monitoring crop maturity for optimized harvesting (Khanal et al., 2017).

Thermal remote sensing has proven effective in detecting diseases and pathogens by capturing the impact they have on plant water stress and stomatal closure. Calderón et al. (2013) used thermal UAV imagery to detect the presence of infection by the fungus *Verticillium dahlia*, finding that the leaf temperature increased and the stomatal conductance reduced when the severity of the disease intensified. The study further revealed that crown temperature and the CWSI are among the best indicators for detecting the fungus *Verticillium dahlia* in the early stages, while other indices such as NDVI and cholorphyll indices showed effectiveness at later stages.

In estimating crop yield, thermal sensors can be combined with red,green,blue (RGB) and/or multispectral sensors. Feng et al. (2020) employed all three types of sensors to investigate the ability of multiple vegetation indices and plant characteristics to estimate crop yield. They found that plant height was the best single yield predictor with a coefficient of determination (R^2) of 0.90. However, the predictive model improved when other features were introduced. Combining temperature measurement with plant height resulted in one of the most accurate models for yield prediction, with an R^2 of 0.94.

Water stress monitoring is one of the most widespread applications of thermal remote sensing, and it is discussed in detail in the following section.

2.2 CWSI

2.2.1 Background

Sustaining an optimal canopy temperature is essential for supporting the metabolic functions of plants. Transpiration plays a vital role in regulating leaf surface temperature (Egea et al., 2017). Through transpiration, liquid water within the plant is converted into vapor and

subsequently released through stomates. The conversion of liquid into vapour requires energy which is absorbed from the leaf surface. As a result, transpiration effectively reduces the temperature of the leaf (Gates, 1964). When a plant suffers from soil moisture shortage, the transpiration rate decreases which causes a rise in the leaf temperature (Testi at al., 2008). An increase in canopy temperature due to water deficiency has multiple negative effects on vital functions of the plant, which can result in a significant decrease in crop yield. Since canopy temperature is related to water stress it can be used as a good indicator to measure the water stress level in plants (Parkash & Singh, 2020).

The mapping of crop water stress variability has gained significant importance for irrigation scheduling. In the 1960s, the primary instrument to measure the vegetative surface temperature was a hand-held thermometer. Tanner (1963) and Fuchs and tanner (1966) used this instrument to assess plant water status and overall plant health. However, introduction of the CWSI by Idso et al. (1981) and Jackson et al. (1981) revolutionized the practical assessment of plant stress levels based on canopy temperature. The CWSI provided a more systemic approach, and the following equation was formulated to calculate it:

$$CWSI = \frac{(Tc - Ta) - (Tc - Ta)ll}{(Tc - Ta)ul - (Tc - Ta)ll} \qquad (1)$$

In this equation, ll represents the lower baseline and ul the upper baseline. T_c represents the canopy temperature in Celsius and T_a the air temperature in Celsius, thus $T_c - T_a$ represents the leaf-to-air temperature difference. The lower baseline denotes the leaf-to-air temperature difference of a plant experiencing no water stress and maintaining an optimal transpiration rate. Conversely, the upper baseline represents a plant under maximum water stress and a low transpiration rate. The value of CWSI typically ranges between 0 and 1, where 0 represents no water stress and 1 maximum stress (Walker & Hatfield, 1983), although negative values have also been reported (Sánchez-Piñero et al., 2022)

After the initial introduction of the CWSI in 1981, multiple ways of calculating CWSI have been introduced. One notable modification was proposed by Jones (1999), who introduced the following formula:

$$CWSI = \frac{T_{canopy} - T_{wet}}{T_{dry} - T_{wet}} \quad (2)$$

In this equation, T_{wet} represents the temperature of completely transpiring leaves T_{dry} refers to the temperature of non-transpiring leaves and T_{canopy} is the measured leaf temperature. Similar to formula (1), the values of the CWSI proposed by Jones (1999) typically fall between 0 and 1. This formula is the most prevailing within water stress studies.

2.2.2 Theoretical, Empirical and Statistical CWSI Approaches

There are generally three main approaches for analyzing water stress using thermal remote sensing: theoretical (CWSIt), empirical (CWSIe) and statistical CWSI (CWSIs). To develop **equation (1)**, Idso et al. (1981) and Jackson et al. (1981) established theoretical limits for the canopy-air temperature difference based on crop energy balance theory. This approach is therefore commonly referred to as CWSIt (Parkash & Singh, 2020). Although this approach has demonstrated successful applications in agriculture (Rud et al., 2014) and viticulture (García-Tejero et al., 2018), it is not without limitations. Due to the requirement of accurate meteorological data and long-term measurements, this approach can be time-consuming and resource-intensive (Zhou et al., 2021).

On the other hand, CWSIe is calculated with artificial reference surfaces which can be obtained by directly measuring the dry reference temperature (T_{dry}) and the wet reference temperature (T_{wet}) (Jones, 1999; Jones et al., 2002). T_{wet} represents fully transpiring leaves and is obtained by spraying water on the leaves (Padhi et al., 2009; Fuentes et al., 2012), while T_{dry} represents non-transpiring leaves and is obtained by covering the leaves with petroleum jelly (Padhi et al., 2009; Poblete-Echeverría et al., 2015). Another option to obtain T_{dry} is by adding a certain value X°C to the air temperature (T_{air}). X is dependant on the vapor pressure deficit (VPD) and usually ranges between 5 and 7 °C (Rud et al., 2014; García-Tejero et al., 2018). However, the

downside of these reference temperatures is that they are easily influenced by the location of the reference leaves and meteorological factors (Bian et al., 2019).

In a study by Santesteban et al. (2017), the empirical approach was successfully applied to assess the potential of CWSI in estimating the patterns of variation in water status within a vineyard. The CWSI values acquired in a single day showed a strong correlation with stem water potential (Ψs) and stomatal conductance (gs) at the time of image acquisition. This finding demonstrates the potential of CWSI in monitoring instantaneous variations in water status within a vineyard.

The last method, CWSIs, utilizes the temperature histogram combined with the air temperature to obtain the references values. Rud et al. (2014) used the mean of lowest 5% of the temperature histogram to obtain $T_{wet.}$, while for T_{dry}, they added 5 °C to the air temperature. This statistical approach has served as a foundation for subsequent variations and adaptations in the field of CWSI estimation.

Park et al. (2017) proposed an adaptation of the statistical approach which they referred to as the adaptive estimation of crop water stress. Their method involves obtaining T_{wet} and T_{dry} values by determining the critical values at the 99% confidence intervals of a Gaussian distribution fitted to the canopy temperature distribution using a Gaussian mixture model. However, relying solely on these critical values for T_{wet} and T_{dry} may introduce significant uncertainty and potential errors.

Bian et al. (2019) presented another alternative approach to the statistical method by incorporating the temperature histogram for both T_{dry} and T_{wet}. They utilized the mean of the lowest and highest 0.5% of the temperature histogram to determine the reference values, introducing their approach as a simplified water stress methodology. Their approach showed more robust results than the empirical approach and the statistical approach using air temperature. In a study conducted by Araújo-Paredes et al. (2022), both the simplified approach and an air temperature model were utilized to estimate and spatialize CWSI in a vineyard. The simplified method involved calculating the average of the 1% extreme temperature values. This approach yielded a slightly higher correlation between CWSI and Ψs compared to the air temperature model. The study demonstrates the potential of the simplified approach in assessing the water status of vines after segmentation, highlighting its usefulness in vineyard

management.

A major advantage of the histogram approach is that it eliminates the need for reference and meteorological measurements, significantly reducing its complexity (Zhou et al., 2021). However, it is important to note that this approach can exhibit biases at the canopy level when applied under different irrigation treatments. Specifically, when T_{wet} is measured on the canopy level with a water deficit treatment, it tends to be higher than the actual value, while the measurement for T_{dry} in well-watered treatments tends to be lower than the actual value. These biases introduce inaccuracies in the CWSI calculation at the canopy level (Zhou et al., 2021).

2.2.3 Canopy Segmentation

In thermal imaging, the index of each pixel represents the temperature of the target. To obtain the value of T_{canopy} with CWSI calculation, pure canopy pixels need to be separated from the background such as sky, soil and random vegetation. Different approaches have been employed to extract pure canopy pixels in thermal imaging, including the use of a temperature threshold, a region of interest (ROI) and a binary mask (Zhou et al., 2021).

The ROI approach has been primarily implemented for ground-based thermal images rather than aerials. When using a ground-based platform, a specific area can be delimited in the middle of the thermal image that mainly includes an area of leaves (Bian et al., 2019). The average temperature of the selected ROI is then considered as T_{canopy}.

The temperature threshold approach relies on the reflectance difference between soil and canopy in thermal imagery to distinguish between them (Santesteban et al., 2017). By analyzing the bi-modal histogram that shows two temperature peaks assigned to soil and canopy, the two types of pixels can be differentiated. However, this method can wrongfully identify mixed pixels at the edges for pure canopy pixels (Rud et al., 2014). Furthermore, the approach is not resistant to spontaneous vegetation between canopy rows. Additionally, the temperature threshold approach struggles in accurately distinguishing canopy under severe water stress. This is because the temperature of stresses canopy can be incorrectly classified as soil, leading to a loss of canopy pixels which influences the reliability of the calculated CWSI (Zhou et al., 2021).

The last approach, the masking technique, involves creating a binary mask that allows to extract canopy in thermal imagery. The binary mask can either be generated using visible (RGB) or multispectral images. By defining the values that represent the canopy, these pixels are assigned a logical value of 1, while non-canopy pixels receive a logical value of 0. Overlaying the mask with the thermal image allows for the extraction of pure canopy pixels. When using RGB imagery, the logical value is determined by color features, since canopy and background colors have distinctive characteristics (Drew et al., 2019). In the case of multispectral images, the NDVI is often utilized to create the binary mask due to its reliable ability to distinguish between soil and vegetation (Zhou et al., 2021). However, a limitation of this technique is that it cannot distinguish natural occurring vegetation from the canopy itself. Another approach is to use the Canopy Height Model (CHM) as the binary mask, which uses the height information of the canopy to separate it from the soil and other vegetation (Cinat et al., 2019). This method offers a straightforward way to differentiate the canopy based on its vertical structure.

2.3 Point Clouds

Compared to 2D data, which can lack depth information and suffer from limitations in representing distances, 3D data offers a more complete and realistic representation of the world. (bron). As a result, the significance of 3D data is growing across multiple fields. In the domains of robotics and autonomous driving, the adoption of 3D data as the prevailing standard is already well-established (Pendleton et al., 2017; Weingarten et al., 2004).

One effective way to represent 3D data is through 3D point clouds, which consist of XYZ coordinates and can contain additional information such as surface normals or RGB values (Bello et al., 2020). Compared to a 3D mesh model, point clouds offer a higher level of precision and the ability to capture fine details such as indents in objects. Point clouds consist of raw data without any interpolation, making them particularly useful for precise measurements within PA (Koenig et al., 2015), while 3D mesh models allow for more enhanced visualization. One of the downsides of point clouds, however, is potential noise disturbance that show up as holes in the model due to transparency or reflectivity (Tabib et al., 2020). Furthermore, automatically identifying and categorizing objects withtin a point cloud can be complex due to the lack of explicit semantic labels. Object recognition algorithms often

rely on additional contextual information or machine learning techniques to classify objects accurately, which can be more challenging with point clouds compared to other data representations like 3D mesh models (Xie et al., 2020).

Despite these challenges, point clouds have proven to be an effective data format in various disciplines, including architecture, engineering, geomatics and Building Information Modelling (BIM) (Bello et al, 2020). In recent years, the potential of point clouds has been demonstrated in PA and PV as well. For instance, Comba et al. (2019) utilized 3D point clouds derived from UAV imagery to assess the Leaf Area Index (LAI) of a vineyard, demonstrating a successful cost-effective alternative compatible with manual measurements. Torres-Sánchez et al. (2021) made use of UAV point clouds to propose a new method for the yield prediction of a vineyard. They successfully developed an unsupervised and automated workflow to detect grape clusters by using point clouds. Weiss & Baret (2017) described a vineyard 3D macro-structure by estimating the row width, height and spacing using UAV point clouds. With optimal flight configuration, accurate estimations were achieved, although the quality of the dense point cloud influences the results.

To expand the capabilities of point clouds, researchers have explored combining point clouds with thermal information in various disciplines. Thermal point clouds, successfully applied in building modeling, offer a valuable tool for analyzing building energy efficiency by providing more extensive information than 2D thermographs (Ramón et al., 2022). Despite their proven worth in multiple disciplines, their applicability within PA, specifically in PV, remains relatively unexplored. This study aims to fill this research gap by utilizing point clouds to measure crop stress and evaluating their potential benefits when integrated into existing PV methods.

3. Methodology

3.1 Research Area

The data was collected from a commercial vineyard located within "Rias Baixas AOP", in "Tomiño, Pontevedra," Galicia, Spain (X: 516989.02, Y: 4644806.53; ETRS89 / UTM zone 29N). The vineyard dates from 1990 and is part of the 'Terras Gauda Winery' and uses the *Vitis vinifera* cv., Loureiro. The vines were planted with 2.5 meters between plants and 3 meters between rows with a NE-SW orientation, with cover crops between the vine rows. They were planted using the Vertical Shoot Position (VSP) system, where vine shoots are trained upward with the fruiting zone below. The plants were grafted on a 196.17C rootstock, which is resistant to active limestone. Appellation of Origin (AOP) rules and practices apply to the vineyard.

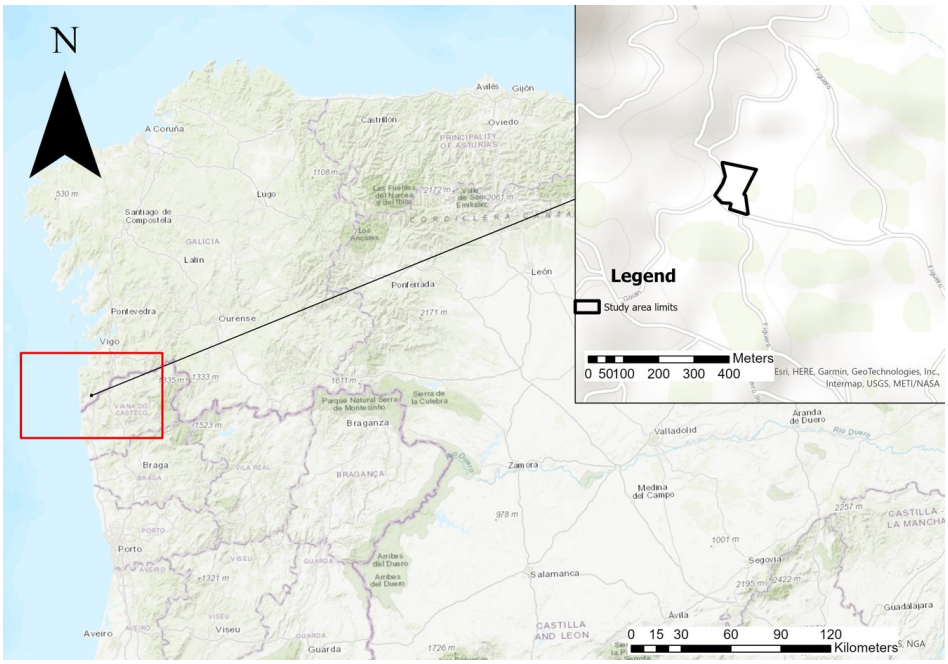

Figure 2. Location of the Vineyard. Coordinates in ETRS89 UTM Zone 29N.

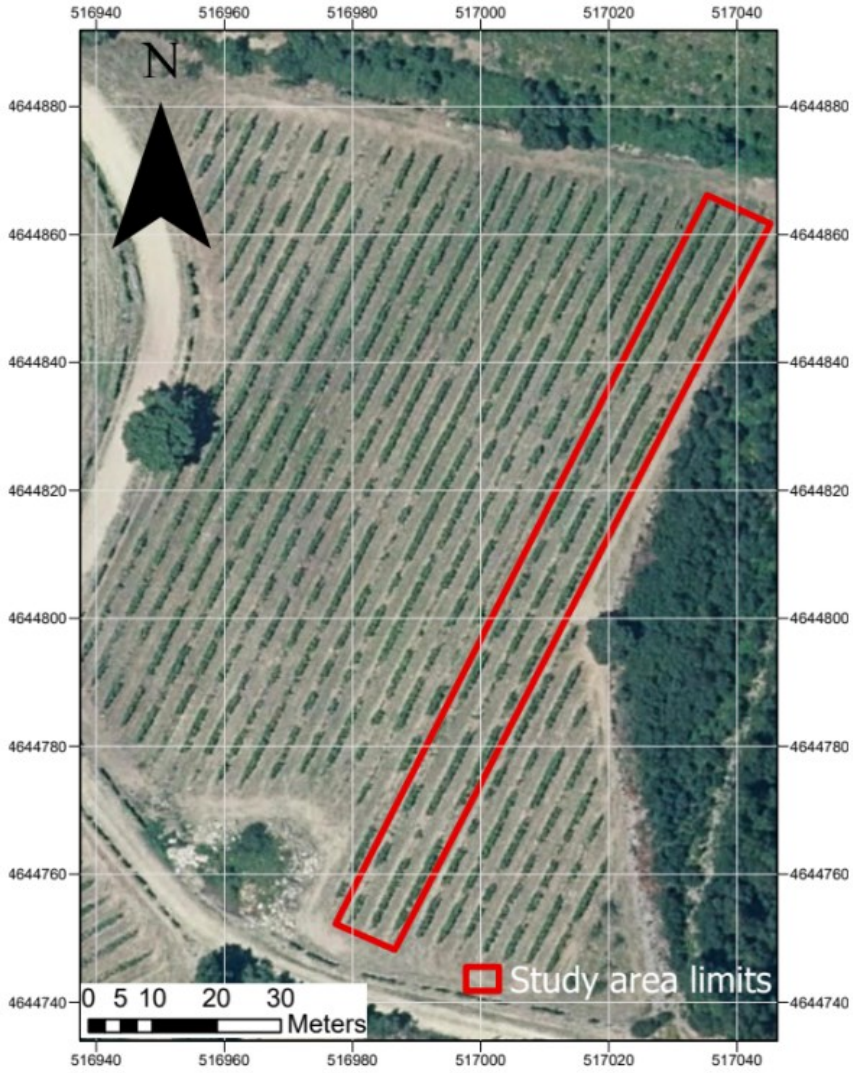

Figure 3. Enhanced view of the study area with the ROI displayed in red. Coordinates in ETRS89 UTM Zone 29N.

3.2 Data

The platform used to acquire multispectral and thermal data was the DJI M300 RTK, a UAV which integrates a flight control system and an FPV camera. It allows obstacle avoidance and six-direction positioning. A MicaSense Altum-PT (AgEagle Sensor Systems Inc., Wichita, Kansas, USA) with multispectral and thermal sensors was used to gather the images. The camera captures images in 7 different bandwidths.

Table 1

Center Wavelengths and Bandwiths of MicaSence Altum-PT. Source: MicaSense, 2022.

Name	Center	Bandwidth
Blue	475 nm	32 nm
Green	560 nm	27 nm
Red	668 nm	16 nm
Red edge	717 nm	12 nm
Near infrared	842 nm	57 nm
Panchromatic	634.5 nm	463 nm
LWIR (Thermal)	10.5×10^3 nm (10.5 μm)	6×10^3 nm

Multiple flights were performed over the study area, for this research two flights are used. The specifications of the flights are shown below.

Table 2

Flight Specifications

Angle	Date	Time	Height
Nadir (0 °)	July 13th, 2022	12:20	30 m
Oblique (30°)	July 13th, 2022	18:30	30 m

Both flights were performed on the same day, with the nadir flight earlier in the day than the oblique flight. The ground control points (GCPs) were located in the vineyard and georeferenced using the Trimble R2 Integrated GNSS system to improve the geometric accuracy of the image mosaicking process.

3.3 Workflow of the Methodology

The following workflow presents the step-by-step process utilized in this study. It serves as a visual guide to gain an overview and understanding of the methodology employed. Each step depicted in the workflow will be elaborated upon in the subsequent sections, providing explanations and justification for their implementation.

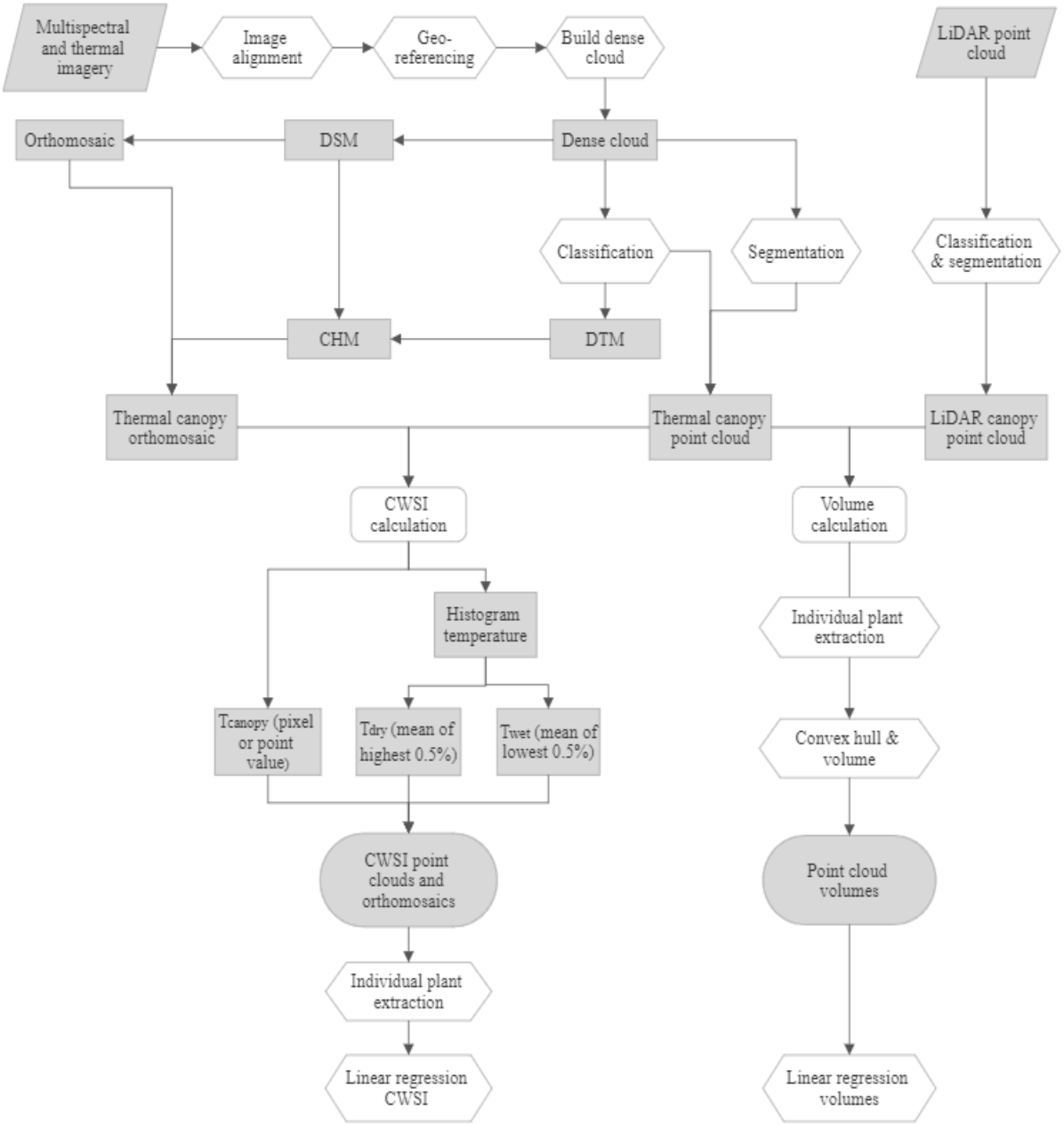

Figure 4. Workflow of the utilized methodology.

3.4 Digital Image Processing

The drone images are processed using Agisoft Metashape Professional commercial software (Agisoft LLC, St. Petersburg, Russia). This software utilizes a SfM algorithm that reconstructs the surface by matching the digital images through automatically identifying related points in every orientation operation.

Figure 5. Workflow of Image Processing in Agisoft Metashape Resulting in the Required Dense Clouds and Orthomosaics.

After uploading the photos into Metashape, the reflectance is calibrated using the calibration panel images found in the folder. Metashape automatically recognizes these calibration images if the meta-data describes their purpose, and saves them in a separate file. If the panel of the camera is has been used before, the calibration information is stored in Metashape's internal database. The next step involves the alignment of the photos, which is done through feature detection and matching algorithms that establish the relative positions of the images. The result of this step is a sparse point cloud that represents the scene. The sparse point is optimized by employing the gradual selection tool. Outliers of the model are deleted in this step and the photo alignment is optimized after each removal, ensuring a more accurate model. Afterwards, the model can be georeferenced with ground control points for higher accuracy. Initially, the model is converted to the local coordinate system, which in this case is ETRS89 UTM zone 29N. The csv file containing the field's GCP coordinates is uploaded, which are displayed as markers by the software. These markers are aligned with the GCPs that can be spotted in the corresponding images. After georeferencing the sparse point cloud, the high-quality dense point cloud can be created. This is done through computer vision algorithms that generate a precise and dense 3D representation of the area based on the sparse cloud. Quality was set to medium due to high computational power that was needed when using the combination of the nadir and oblique flight. Again, the model is optimized by deleting outlying points. Afterwards, a Digital Surface Model (DSM) is built by interpolating the dense cloud to produce a continuous surface that represents the topography of the scene. Finally, the orthomosaic is created by projecting the images onto the DSM. The resulting image is an orthorectified mosaic

of the scene that seems captured from a single perspective at a fixed height.

3.5 CWSI Orthomosaics

The subsequent sections of the methodology are organized according to the research questions addressed in this study. As the first research question has been covered in the literature review, this section begins with research question 2. Specifically, this section focuses on the first part of RQ2, which deals with how thermal UAV data can be utilized to generate CWSI orthomosaics.

The CWSI, which relies on canopy temperature, is a widely adopted indicator for assessing plant water stress and mapping spatial variability (Bahat et al., 2021). In this study, the thermal band of the multispectral camera is utilized to evaluate the surface temperature of the vineyard's canopy. To derive accurate temperature values specifically related to the canopy, it is essential to extract pure canopy pixels while eliminating noise sources such as soil and grass. This process involves the creation of a binary mask, utilizing ArcGIS Pro 3.0.2 (ArcGIS™ software by Esri®, Inc.). Initially, an NDVI mask was employed, where higher values represent vegetation and lower values represent soil. However, due to the presence of inter-row vegetation in the research area, this approach proved inadequate, as depicted in **Figure 6.**

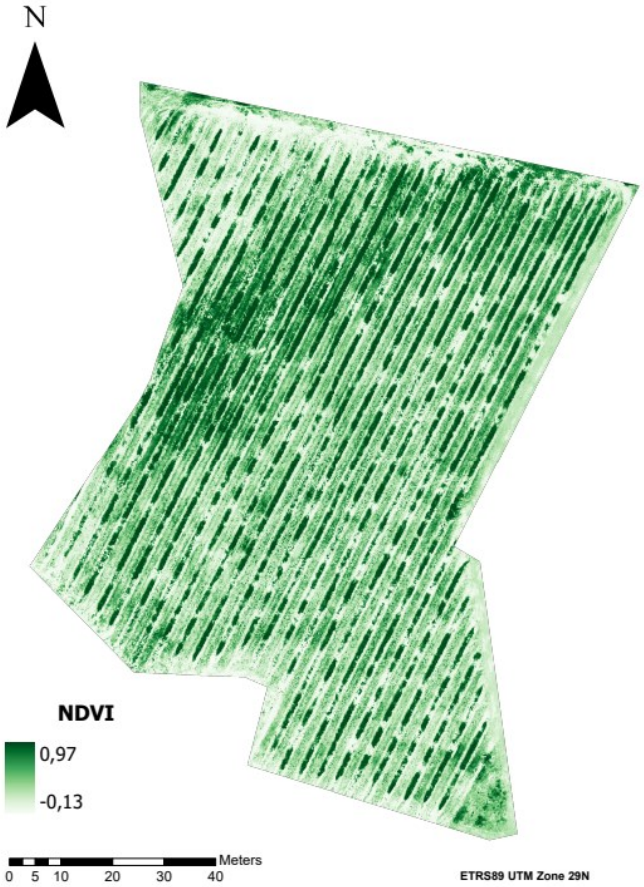

Figure 6. NDVI map of the vineyard showing inter-row vegetation.

To overcome the aforementioned challenge, this study utilizes a CHM as an alternative approach. The CHM plays a crucial role in accurately extracting canopy pixels while effectively separating plant rows from the ground rows situated between the vines.

The creation of the CHM involves the generation of a DSM and a Digital Terrain Model (DTM) using Metashape software. The DSM is generated by incorporating all the points from the point cloud, resulting in a file that represents the height of various objects within the study area. Simultaneously, the DTM is constructed by initially classifying the ground points within Metashape.

Subsequently, the CHM is derived by subtracting the DTM from the DSM. This process ensures that the CHM specifically captures the vertical extent of the canopy while excluding the ground elevation. Afterwards, a threshold layer is created using a chosen threshold value of 0.5 meters. In this context, pixels with heights exceeding 0.5 meters are assigned a value of 1, indicating their association with the canopy, while pixels below this threshold are assigned a value of 0.

The selection of a 0.5-meter threshold is based on the understanding that spontaneous vegetation typically does not attain this height, while all the cultivated plants in the vineyard are at least 0.5 meters tall. Consequently, this threshold effectively distinguishes the canopy vegetation from other objects and vegetation in the study area. A visual representation of the CHM is displayed in **Figure 7.**

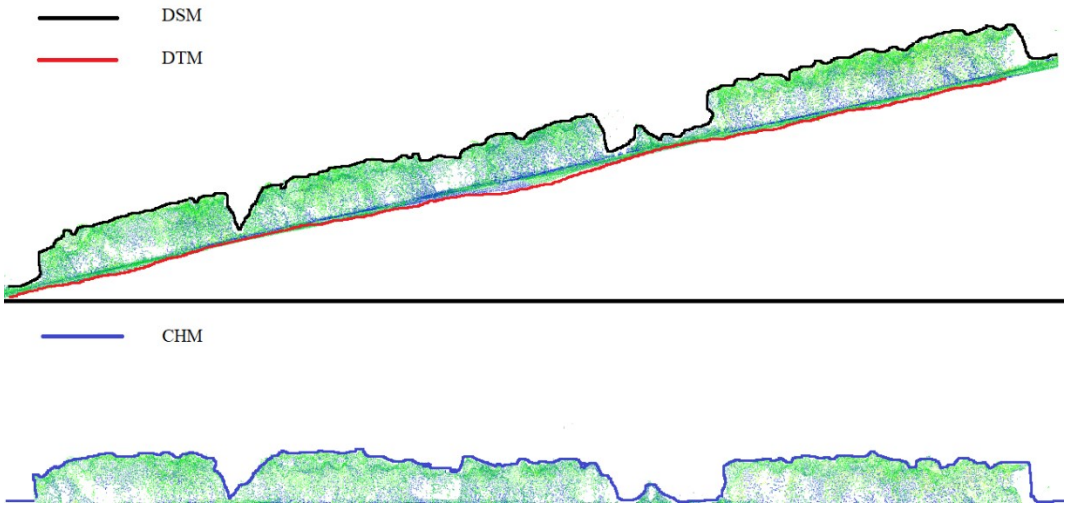

Figure 7. Obtaining the CHM from a vineyard, utilizing the DSM and DTM.

Following the generation of the binary mask layer, the thermal layer of the orthomosaic is divided by the mask layer. This operation produces a new layer exclusively containing temperature values corresponding to the canopy pixels. To ensure proper unit conversion, these temperatures are divided by 100 and then subtracted by 273.15, effectively converting the values from Kelvin to Celsius. The workflow depicting the step-by-step procedure for the canopy extraction process is illustrated in **Figure 8.**

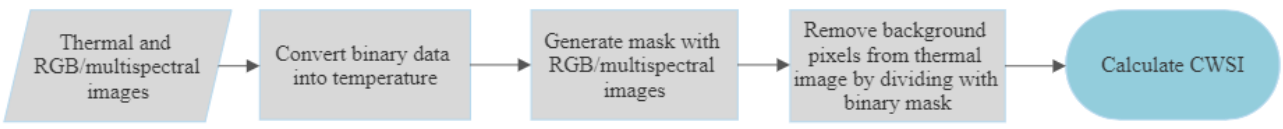

Figure 8. Workflow for image processing for CWSI calculation.

The final step, calculating the CWSI, is done by applying **equation (2)**. In the CWSI calculation, the measured temperature of the canopy pixels is compared to the lower and upper limits representing a non-stressed leaf (T_{wet}) and a leaf in maximum stress (T_{dry}), respectively. As discussed previously, various approaches exist for determining the reference temperatures T_{wet} and T_{dry}.

Initially, an empirical approach following research such as Matese et al. (2021) was employed in this study. This involved coating vines with petroleum jelly to obtain the dry reference temperature, while plants were sprayed with water to obtain the wet reference temperature. However, a limitation was identified when calculating CWSI values using these references. The reference measurements were obtained in a shaded area, while the orthomosaics encompass sunlit areas with higher temperatures. Consequently, the CWSI models generated from these references produced inaccurate results, with values significantly exceeding the expected 0 to 1 range.

To overcome this challenge, a modified approach known as the simplified CWSI approach (Bian et al., 2019; Araújo-Paredes et al., 2022) is employed. In this method, the temperature histogram is utilized to determine the wet and dry reference values. Specifically, the wet reference is calculated by averaging the lowest 0.5% of the histogram, while the dry reference is obtained by averaging the highest 0.5% of the histogram. This modification enables a more accurate assessment of water stress by aligning the reference values with the temperature distribution observed in the orthomosaics.

3.6 CWSI Point Clouds

This section focusses on the second part of RQ2, which explores the utilization of thermal UAV data in generating CWSI orthomosaics. When creating the orthomosaic using Metashape, the software generates point clouds for all seven bands, including the thermal band captured by the camera. This built-in capability of Metashape simplifies the process of generating thermal point clouds, enabling their direct application in research studies (Grechi et al., 2021; Guilbert et al., 2020).

To classify the thermal point cloud and separate the canopy from the soil and trunks, Metashape offers useful tools. The ground points of the point cloud were previously classified to create the Digital Terrain Model (DTM). Metashape's "classify ground points" tool automates this process. The software divides the dense cloud into cells and detects the lowest point in each cell. By triangulating these lowest points, an initial estimation of the terrain model is obtained. New points are then assigned to the ground class if they fall within a specified distance and angle from the terrain model. These parameters, the maximum angle, and distance, can be adjusted to optimize the classification.

After exporting the classified point cloud as an XYZ file, specifically selecting the canopy class, the point cloud data is stored in a format that enables the reflectance values of each band to be stored in separate columns. This format facilitates the subsequent analysis of the thermal point cloud. The exported point cloud is then imported into CloudCompare (version 2.12.1) [GPL software], an open-source software renowned for its capabilities in manual editing and rendering of 3D point clouds.

Within CloudCompare, the reflectance values of the thermal point cloud are stored as a scalar field within the file, ensuring that the spectral information is preserved for further analysis. The software provides tools for refining the point cloud by performing noise filtering techniques, which enhance the accuracy and quality of the data. This step aids in removing unwanted outliers from the point cloud, resulting in a cleaner representation of the canopy structure.

Additionally, the final step of the point cloud classification involves manual intervention. Points that do clearly not belong to the canopy (soil or trunks) are carefully removed from the dataset. This manual deletion process ensures that the resulting point cloud is the most accurate representation of the canopy structure.

Finally, the temperature values in the point cloud are converted from Kelvin to Celsius using the arithmetic tool provided by CloudCompare. The resulting temperature values are then used to calculate T_{wet} and T_{dry} based on the temperature histogram of the point cloud. With these reference values, the CWSI values can be computed for each point in the point cloud using **equation (2)**. This process ultimately generates a CWSI point cloud that represents the water stress levels across the research area.

3.7 Statistical Analysis

This section addresses research questions 4 and 5, which are as follows:

- *What are the differences between the data models?*
- *What is the influence of the flight angle on the CWSI calculation?*

3.7.1 Individual Plant Extraction

To enable meaningful statistical comparisons, individual plants within the research area are isolated. This is achieved by creating a grid in ArcGIS Pro, where a rectangular polygon is defined around the research area and subsequently divided into multiple equal areas. A selection of the rectangular segments is then performed in a manner to ensure an equal distribution across the study area. Furthermore, smaller segments of canopy are not selected to avoid bias in CWSI and volume calculation, resulting in 51 polygons, or plants.

The same grid is applied to all orthomosaics and point clouds, ensuring consistent segmentation of plants for subsequent analysis. The grid-based plant isolation process is depicted in **Figure 9** for both nadir orthomosaic and point cloud data.

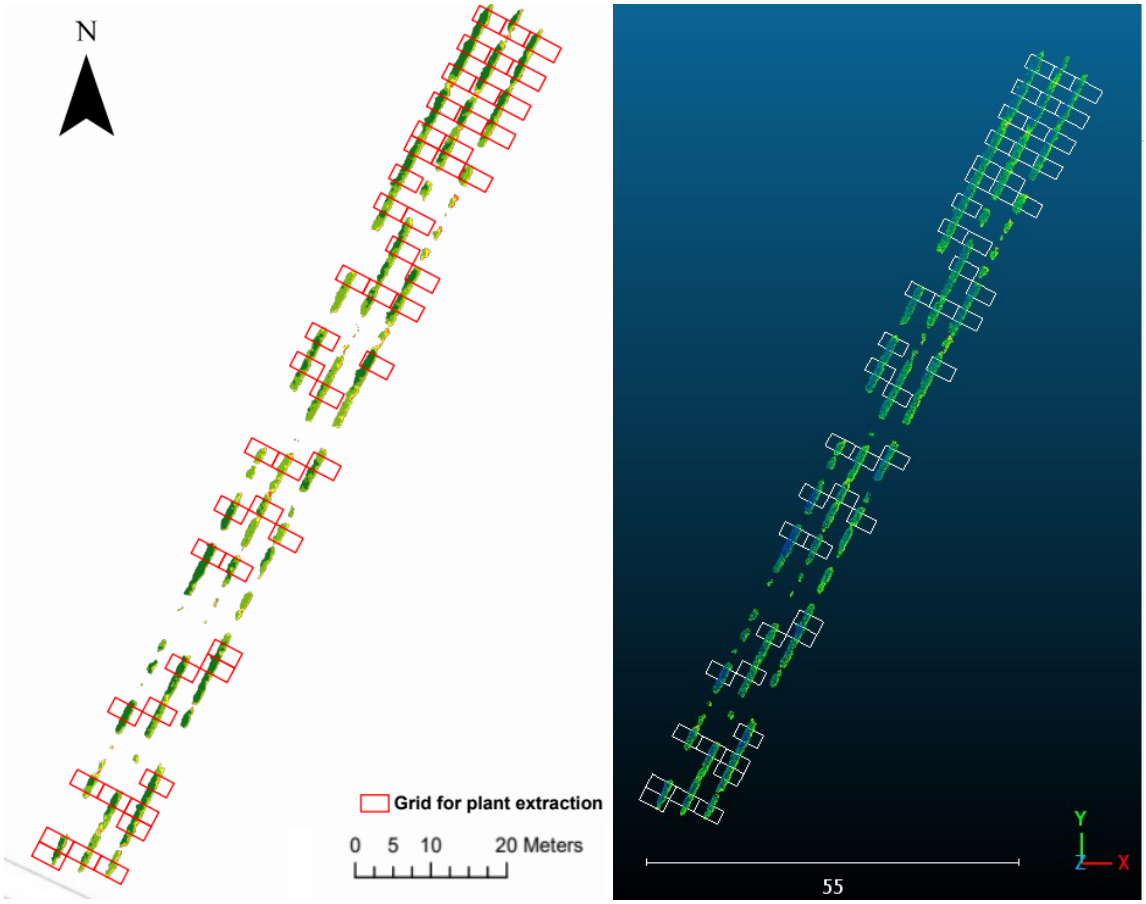

Figure 9. Grid used to isolate individual plants. The left image illustrates the nadir orthomosaic, while the right image showcases the nadir point cloud. Coordinates are represented in ETRS89 UTM Zone 29N.

It should be noted that the grid does not precisely correspond to actual individual vines in the vineyard due to variations in vine sizes and locations. However, the grid ensures that each "plant" is consistently isolated, enabling valuable analysis between different data models. Furthermore, the length of the polygon was set slightly over 2 meters to approximate the size of the actual plants.

3.7.2 Flight Angle Influence

In this study, both nadir and oblique flights are employed. Additionally, a combined dataset is created by merging the images from both flights to generate orthomosaics and point clouds. The aim is to investigate the influence of flight angle on the CWSI calculation. Previous studies by Li et al. (2022) and Lin et al. (2021) have demonstrated the potential of oblique imagery for point cloud analysis in agriculture, as it can capture the sides and bottom of canopies more effectively than nadir flights. Furthermore, combining nadir and oblique flights resulted in more accurate outcomes compared to studying either angle individually. Considering the focus of this research on the potential of point clouds to capture a larger portion of the canopy, including the oblique flight is justified.

3.7.3 Collecting Statistics

After isolating the plants in all orthomosaics and point clouds, statistical analysis is performed to extract insights from the data models and evaluate the influence of the flight angle. For orthomosaics, zonal statistics in ArcGIS Pro is utilized. However, since zonal statistics only accepts integers, the CWSI values are first multiplied by 100 and converted into integers to preserve precision. This process generates a table containing the mean CWSI values of each plant for all three orthomosaics.

For point clouds, CloudCompare does not provide a built-in zonal statistics function. Therefore, Python 3.10 is utilized to calculate the average CWSI values for each plant in the point clouds, which are stored in text files. The Python code loops through the point clouds, computes the average CWSI value, and saves the results in an .xlxs file. Finally, the statistics from different flights and data models are consolidated into a single file, which is then ready for linear regression analysis.

3.7.4 Linear Regression Analysis

Linear regression analysis is performed to compare the orthomosaic and point cloud data models for each flight. This analysis aims to identify differences between the two data models. Since both models use the same data and undergo similar processing steps, their values

should exhibit some similarities. However, due to the point cloud's ability to capture more information, differences are expected.

To further investigate the disparity between orthomosaics and point clouds, the same analysis is conducted, but this time the top of the canopy is segmented. If R^2 increases after segmentation, it indicates that the side and bottom portions of the canopy contribute to the differences in the orthomosaic. This finding would suggest that the CWSI point cloud provides a more detailed representation than the orthomosaic. In addition to comparing the orthomosaic and point cloud data models, linear regression analysis is also performed between the different flight angles. This analysis aims to explore the influence of flight angles on the CWSI calculation.

3.7.5 Volume calculation

To further explore the influence of the flight angles, the volumes of each plant in the point clouds are calculated and compared to the volumes derived from a LiDAR point cloud of the research area. The LiDAR dataset serves as ground-truth data due to its superior accuracy and point cloud density. By comparing the volumes, the most accurate point cloud creation method (nadir, oblique, or combined) can be determined. Although this comparison does not directly assess the accuracy of the CWSI calculation, it provides insights into how well the point cloud captures the canopy geometry, which, in turn, contributes to more accurate results in subsequent analysis, such as CWSI calculation.

Python is utilized to calculate the volumes for all the point clouds. The LiDAR point cloud undergoes the same segmentation and classification steps as the other point clouds. The Python code loops through the plants and calculates their volumes using the convex hull method.

The convex hull method is a geometric algorithm used to calculate the volume of a three-dimensional object or point cloud. It involves constructing the smallest convex shape that encloses all the points of the object or point cloud. The resulting convex hull represents the outer boundary of the object (Baíllo & Chacón, 2021). To calculate the volume using the convex hull method, the algorithm computes the total volume of the convex shape by dividing it into smaller tetrahedrons or pyramids. The volume of each tetrahedron or pyramid is then

calculated based on its base area and height. By summing up the volumes of all the tetrahedrons or pyramids, the total volume of the object or point cloud enclosed by the convex hull can be determined.

Once the volumes of each plant have been calculated and stored in an Excel file for all the flights, the next step is to perform linear regression analysis between the volumes derived from the three flights (nadir, oblique, and combined) and the volumes obtained from LiDAR data. By conducting linear regression, it can be assessed which flight provides the most consistent and accurate volume estimation, aiding in the evaluation of the quality and reliability of the geometry of the point clouds.

Validation of remotely sensed CWSI values is typically conducted using ground-truth data, which involves direct measurements of plant physiological parameters such as leaf water potential (Ψleaf) and stomatal conductance (gs). These parameters have a strong correlation with CWSI and serve as reliable indicators for validation purposes (Zhou et al., 2021). However, in this research, the unavailability of expensive instruments like the pressure chamber for Ψleaf measurement and leaf porometer for gs measurement limits the direct validation of CWSI values. Despite this limitation, the methodology employed in this study aims to overcome this challenge and provide an alternative approach for evaluating the accuracy of CWSI through the data models and analysis described.

4. Results

In the first section of the results, the orthomosaics and point clouds generated using ArcGIS Pro, CloudCompare, and Metashape are visualized. This section aims to showcase the process of producing the final products and provide an overview of the temperature and CWSI distribution within the study area for each of the orthomosaics and point clouds. In the second section of the results, the statistical analysis between the different flights and data models is shown to gain more insight into the obtained values.

4.1 Visual Results

4.1.1 Orthomosaics

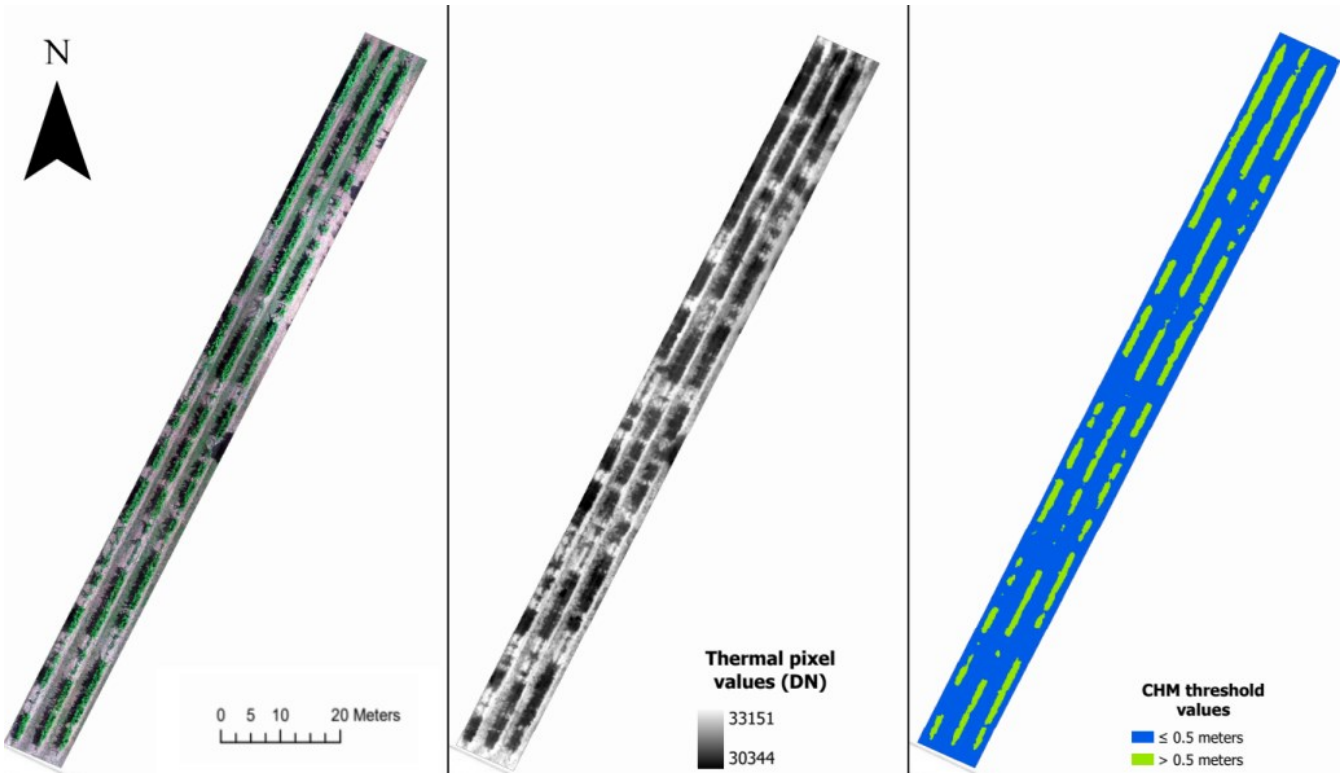

Figure 10. Orthomosaics of the study area from the nadir flight in RGB (left), thermal (middle) and the CHM threshold (right). Coordinates in ETRS89 UTM Zone 29N.

Figure 10 shows the orthomosaic in RGB, the thermal band in raw pixel values and the CHM threshold layer. The blue parts of the threshold layer represent non-canopy and contain 0 values and the green parts represent canopy which contain 1 values. The thermal layer (middle) is divided by this threshold layer to obtain the canopy-only pixels of the thermal layer. This layer is then converted into temperature values (Celsius), after which the CWSI layer can be created. The figure serves to illustrate how the CWSI layers are obtained, hence only the nadir flight is shown here, since the other flights follow the same process. The obtained CWSI orthomosaics for the different flights are shown below in **Figure 11.**

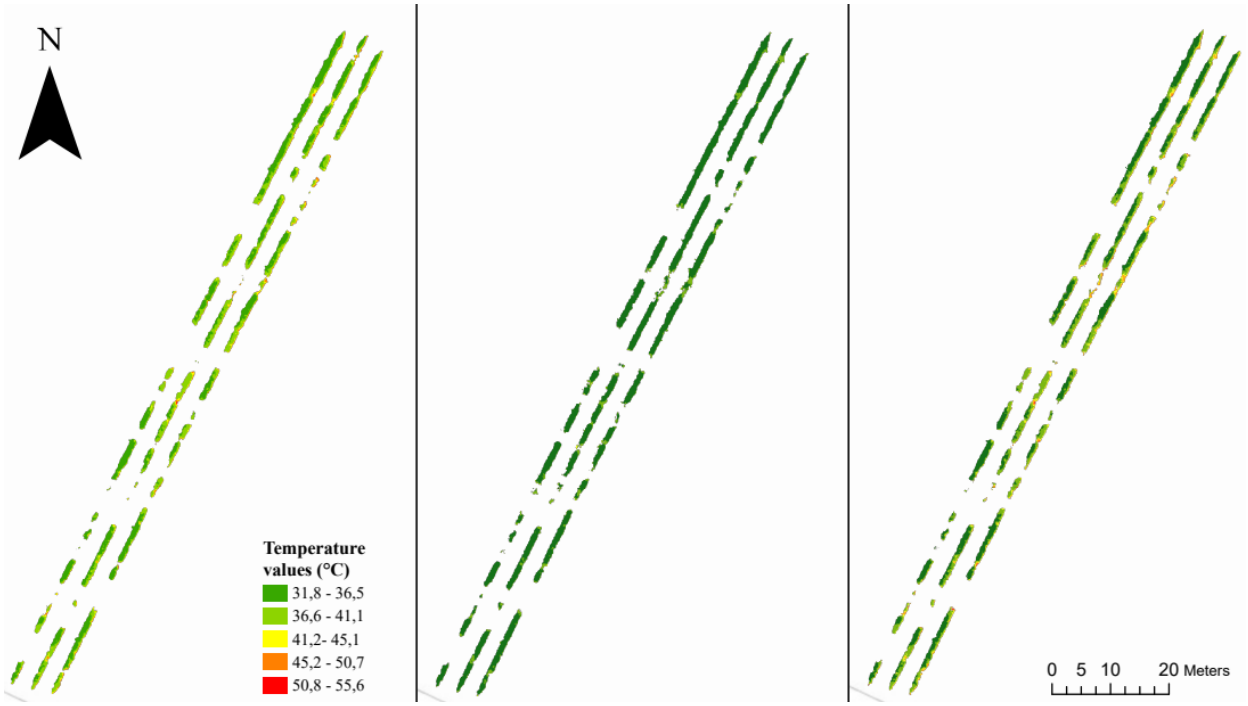

Figure 11. Orthomosaics of temperature values of the nadir flight (left), the oblique flight (middle) and the two flights combined (right). Coordinates in ETRS89 UTM Zone 29N.

The temperature variation between the nadir and oblique flights is most evident, with the former showing significantly higher temperatures. Specifically, the maximum temperature recorded during the nadir flight was 54.4 °C, whereas the oblique flight recorded only 44.8 °C. Consequently, the oblique orthomosaic is predominantly green and lacks any yellow or red elements. This temperature difference can be attributed to the difference in air temperature during the flights. Air temperature data was collected at 10-minute intervals from the nearest weather station, which is part of the official network of weather stations maintained by the

Meteorological Observation and Prediction Unit of the Government of Galicia. The nadir flight took place at 12:20, when the temperature was 35.9 °C, while the oblique flight was conducted at 18:30 when the temperature was 27.9 °C. Furthermore, all the orthomosaics indicate higher temperatures on the east side of the canopy than on the west. This outcome could be attributed to the east side receiving the most intense sunlight, leading to a temperature difference that could explain this. These temperature values resulted in the following CWSI orthomosaics.

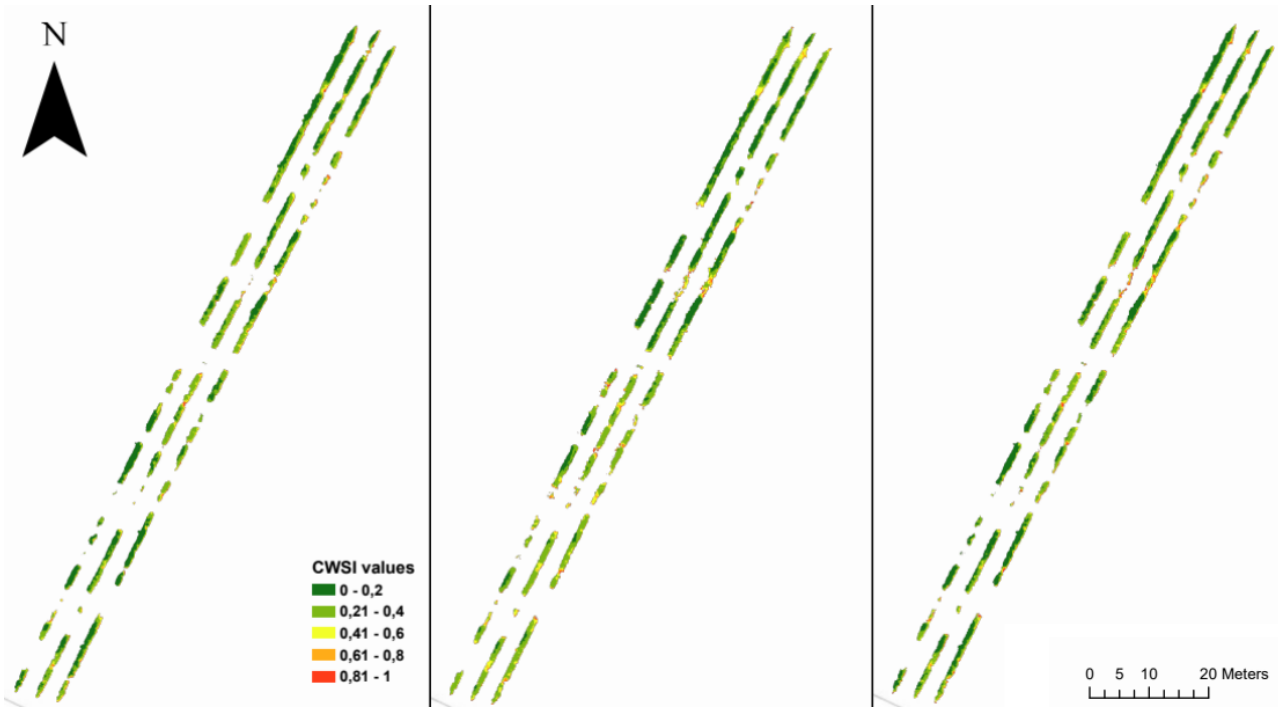

Figure 12. Orthomosaics of CWSI values of the nadir flight (left), the oblique flight (middle) and the two flights combined (right). Coordinates in ETRS89 UTM Zone 29N.

.

Despite the oblique flight capturing lower temperatures, the resulting CWSI orthomosaics exhibit similar trends, with the lowest values observed in the north and slightly higher values in the south of the vineyard. This similarity can be attributed in part to the CWSI calculation process, which normalizes values between 0 and 1. However, the statistical analysis is

necessary to determine the actual similarity of the CWSI values. Across all three orthomosaics, the east side of the canopy consistently displayed higher CWSI values. While some CWSI values below zero or above 1 were observed in both flights, they are not included here as they are minimal. These irregular values beyond the expected range of 0 to 1 occur due to the CWSI calculation methodology, which employs histograms. The reference values for CWSI calculation are the averages of the top and bottom temperature values, hence certain pixels contain higher or lower values than this average.

4.1.2 Point clouds

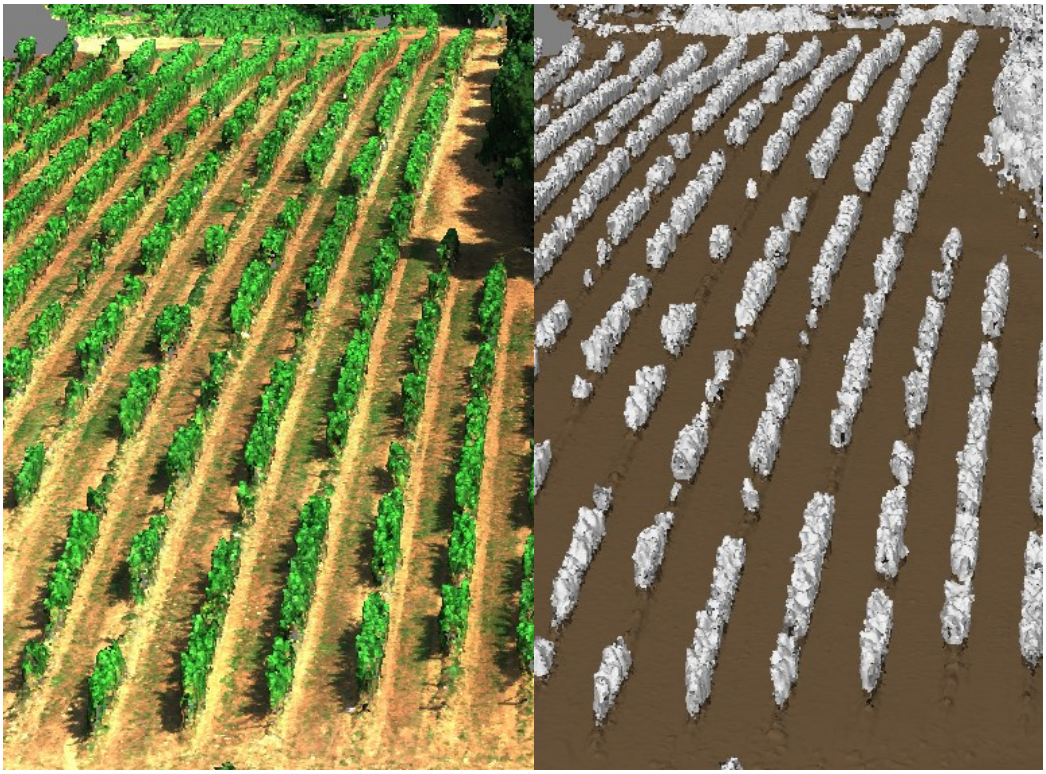

Figure 13. Point clouds of nadir flight in RGB (left) and the classified version (right).

The image on the left displays the RGB point cloud captured during the nadir flight of the entire field. The image on the right shows the same point cloud, with the ground points classified as brown and the canopy points as white. Both images depict a larger portion of the field beyond the study area, as segmentation has not been performed yet. The white points were exported as a text file and subsequently uploaded into CloudCompare, where additional processing was carried out to generate temperature data. Finally, the CWSI point cloud, illustrated in **Figure 14**, was produced through further processing.

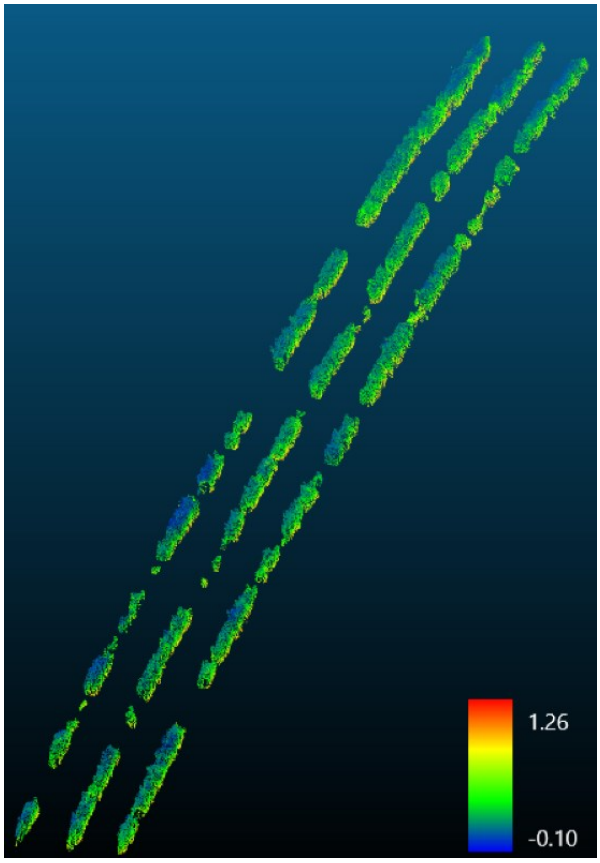

Figure 14. CWSI point cloud of nadir flight.

The figure displays the CWSI point cloud obtained from the nadir flight. The point cloud was subsequently segmented using the same file that was used for the orthomosaic, which resulted in individual plants. Only the nadir flight is shown in this figure since displaying the entire map would make it challenging to discern any differences between the flights. To compare the various flights, the same plant (plant 1) from each flight is presented in **Figure 15.**

Figure 15. CWSI point cloud of plant 1 from the nadir flight (left), oblique flight (middle) and the combined flights.

All three flights display a comparable pattern, with lower CWSI values at the top and higher values towards the bottom of the canopy. Across all flights, the highest CWSI values can be observed at the bottom of the canopy on the east side. However, the nadir flight exhibits slightly higher values on the west side of the canopy, where the other two flights show lower (blue) values. Furthermore, the oblique and combined flight point clouds offer more comprehensive coverage on the sides and particularly at the bottom.

4.2 Statistical results

The statistical results are presented in the following manner. In the first section, the general statistics are provided, which include the values of the data models pertaining to temperature, CWSI values and quality. These statistics offer an overview and description of the data, allowing for a better understanding of the overall characteristics and trends within the datasets. The second section focusses on the linear regression analysis between the CWSI values and the last section deals with the volume calculations.

4.2.1 General statistics

The following results provide insight into the general statistics of the data models regarding the temperature, CWSI values and the number of points/pixels. **Table 3** shows that the maximum temperature recorded across all flights and data models is high, particularly for the nadir and combined flights. These higher temperature values consequently lead to higher T_{dry} values. The maximum temperature and T_{dry} exceed the anticipated range based on previous studies (Bian et al., 2019; Araújo-Paredes et al., 2022). These values suggest the possibility of misidentifying some soil pixels and points as canopy pixels. However, it is important to note that the average temperature values align more closely with what is expected, indicating that these high temperatures are mostly outliers.

Table 3

General Statistics of Data Models

Flight	Data model	Min temp	Max temp	Mean temp	St. Dev. temp	Min CWSI	Max CWSI	Mean CWSI	Twet	Tdry	St. Dev CWSI	Pixels/points (N)
Nadir	Ortho	31.9	54.4	37.9	3.42	-0.04	1.21	0.29	32.5	50.7	0.19	66,945
	PC	31.7	56.2	38.9	3.69	-0.10	1.26	0.30	33.5	51.5	0.20	215,199
Oblique	Ortho	31.4	44.8	34.9	1.86	-0.04	1.30	0.31	31.8	41.9	0.19	47,717
	PC	31.0	43.2	35.2	1.64	-0.09	1.20	0.35	31.9	41.3	0.17	181,372
Combined	Ortho	31.8	55.5	38.3	3.83	-0.04	1.19	0.30	32.5	51.8	0.20	53,315
	PC	31.1	55.0	36.4	2.72	-0.06	1.27	0.23	32.2	50.1	0.15	208,687

The oblique flight has the lowest number of pixels/points for both the point clouds and the orthomosaic, while the nadir flight contains the highest. Although the combined flights create data models with images from both flights, these results indicate that this doesn't necessarily lead to more points or pixels. The most noticeable difference is the lower maximum temperature for the oblique flight in both the orthomosaic and the point cloud, with its mean temperature also being lower than that of the other two flights. Conversely, the CWSI values are highest in the oblique flight for both the point cloud and the orthomosaic.

For the nadir and combined flights, the minimum and maximum temperature values of the point cloud are lower and higher, respectively, than those of the orthomosaic. This trend is also observed for the CWSI values. It is expected that the point cloud would have a wider temperature and CWSI range, as it uses the same data but is more complete. However, for the oblique flight, the orthomosaic shows a higher maximum temperature and CWSI value instead of the point cloud.

4.2.2 Linear regression

To further understand the differences between the orthomosaics and point clouds, statistical analysis using the mean CWSI values of each plant from each data model and flight was conducted. The point clouds and orthomosaic were segmented into individual plants and their mean CWSI values were calculated and stored in an xlsx file. Linear regression was performed between the means to identify any differences between the data models. **Figure 16** displays the results of the linear regression analysis between the orthomosaic and point cloud of each flight.

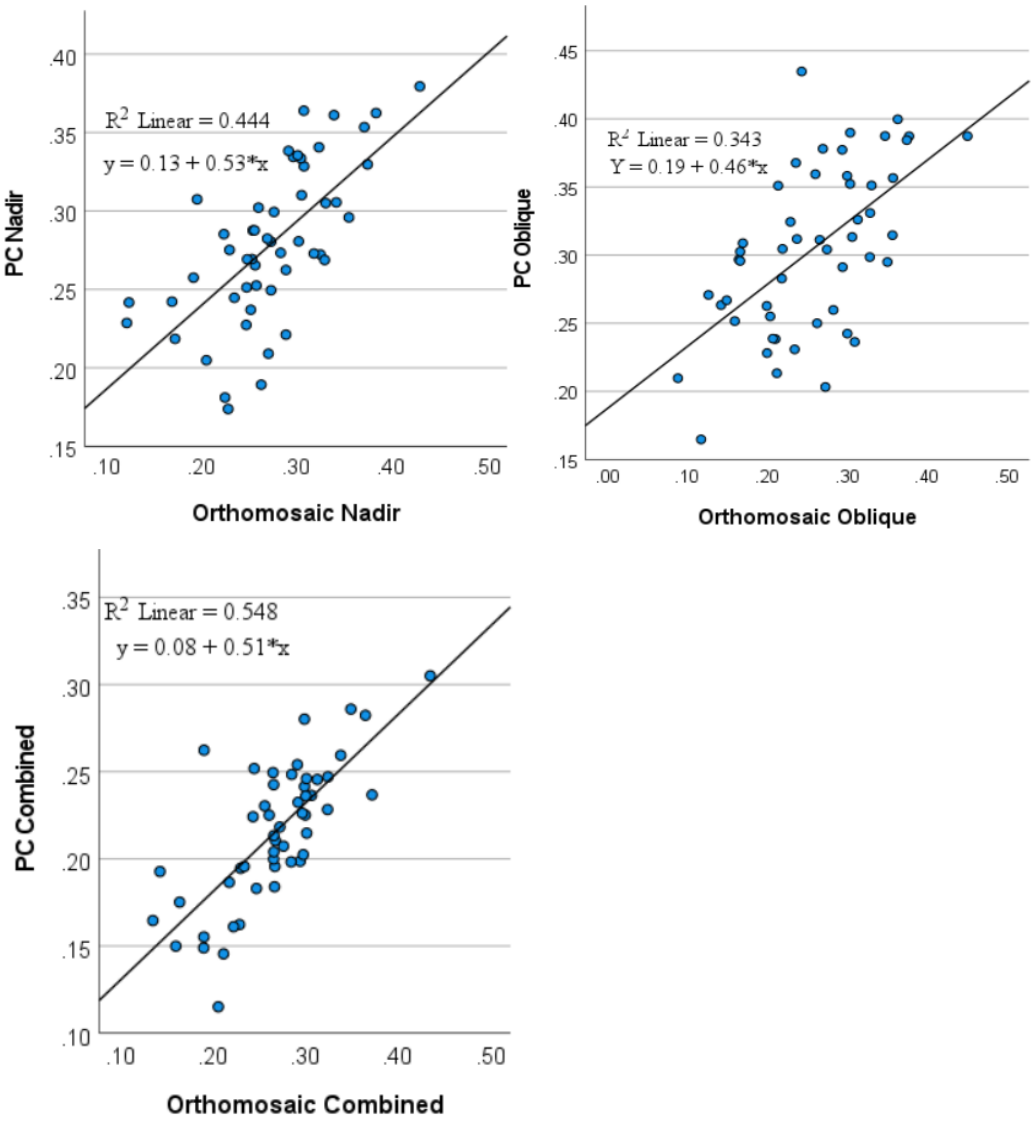

Figure 16. Linear regression between the CWSI orthomosaic and CWSI point cloud of the nadir flight (left top), the oblique flight (right top) and the combined flights (bottom).

The R^2 values indicate a low model fit and a discrepancy between the obtained CWSI values of the data models. It is assumed that the point cloud contains more detailed information compared to the orthomosaic, suggesting that there should be a noticeable difference between the two data models. If the R^2 values were close to 1, it would imply that the point cloud and orthomosaic are very similar, raising the question of their additional value. However, these numbers alone do not provide information about whether the difference in values is caused by the additional CWSI values present in the point clouds.

To further analyze this, the top of the point clouds was segmented, and the regression analysis was repeated using only the top portion. Since the orthomosaic utilizes only the values from the top of the canopy, this approach should lead to an increase in R^2.

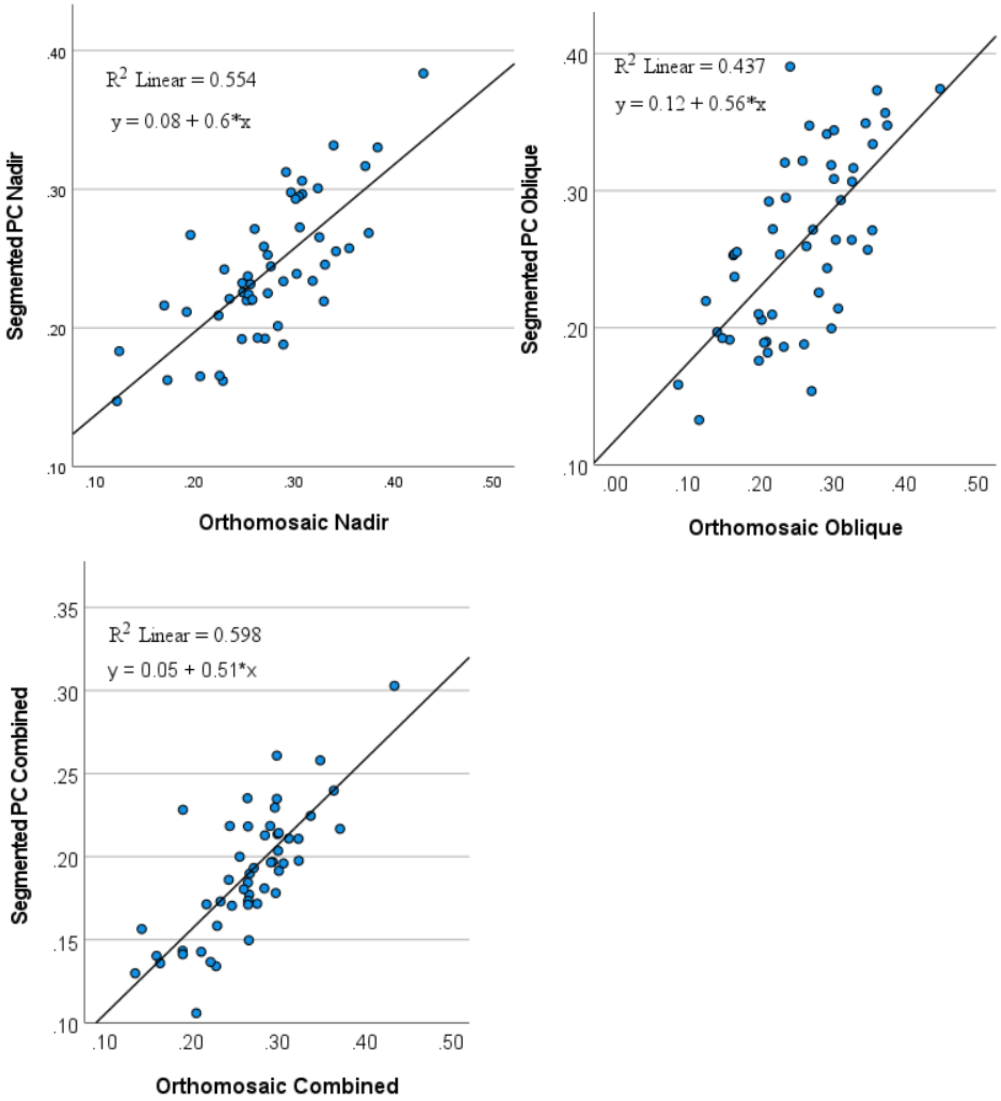

Figure 17. Linear regression between the CWSI orthomosaic and segmented CWSI point cloud of the nadir flight (left top), the oblique flight (right top) and the combined flights (bottom).

Figure 17 demonstrates significant increases for all flights following the segmentation of the top of the point clouds. This finding suggests that the discrepancy between the orthomosaic and point cloud values is partially attributable to the additional information contained in the point clouds regarding the side and bottom of the canopy. However, despite these improvements, the R2 values remain relatively low. This indicates that there are other factors influencing the CWSI calculation when utilizing the point cloud approach.

To further explore the variations observed among different flights and data models, the subsequent figure presents linear regression results comparing flights within the same data model. For instance, the top left scatter plot shows the linear regression between the nadir and oblique orthomosaic.

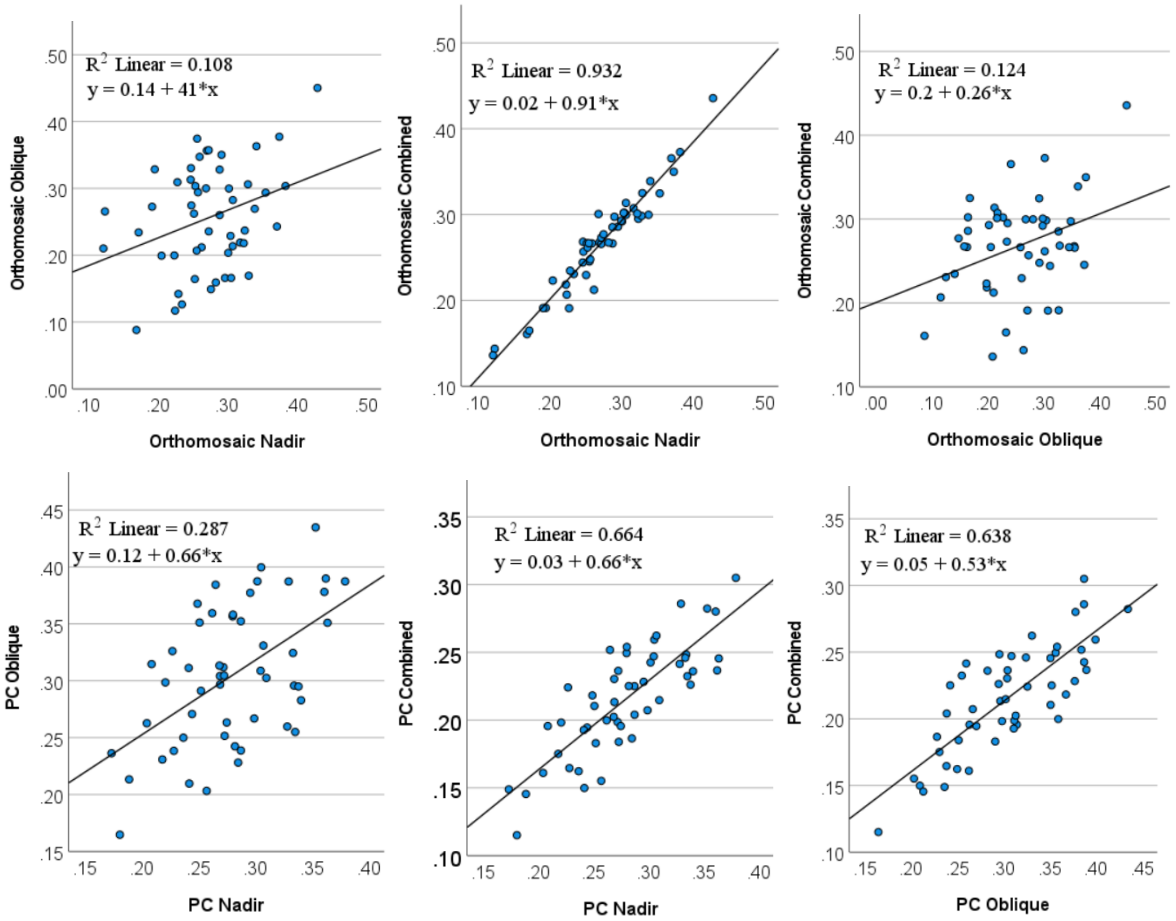

Figure 18. Linear regression between different flights of orthomosaics (top) and point clouds (bottom).

Firstly, it is striking to observe the low R^2 value when comparing the CWSI values obtained from the nadir and oblique flights during the point cloud analyses. This low R^2 value indicates a significant variability between these two flight types. Given that both flights were conducted on the same day, one would expect the CWSI values to be more similar. In contrast, the R^2 values for the combined flights (nadir + combined and oblique + combined) are considerably higher at 0.66 and 0.64, respectively. The similarity of these R^2 values suggests that the point cloud derived from the combined flights contains roughly equal contributions from both the nadir and oblique flights.

However, a different pattern occurs when considering the orthomosaic datasets. The R^2 value for the nadir + combined orthomosaic is 0.93, while for the oblique + combined orthomosaic, it is only 0.12. This stark difference indicates that the orthomosaic dataset derived from the combined flights predominantly includes values obtained from the nadir flight, with minimal representation from the oblique flight. This suggests that oblique imagery enhances the analysis when utilizing 3D point clouds, but its impact is negligible when working with orthomosaics Moreover, the R^2 values for the nadir and oblique flights within the orthomosaic dataset are both very low, at 0.11. This further emphasizes the substantial disparity in the CWSI values between the two datamodels.

4.2.3 Volume calculation

The subsequent section presents the results obtained from volume calculations performed on the point clouds derived from various flights, as well as the LiDAR point cloud. The volume measurements from the LiDAR point cloud are considered as ground-truth data due to its high accuracy. While the accuracy of volume calculations does not directly provide information about the CWSI calculation, it demonstrates how well the point clouds capture the actual geometry of the vineyard. Thus, a more accurate representation of reality leads to more precise results.

The LiDAR point cloud underwent classification and segmentation using the same methodology and parameters as the other point clouds. The initial height and volume calculations are provided in **Table 4.**

Table 4

Average Heights and Volumes of Point Clouds

Flight	Mean height	Mean volume
Nadir	1.46	2.35
Oblique	1.52	2.54
Combined	1.51	2.54
LiDAR	1.78	3.09

Through these calculations, the following linear regression results between the point clouds and the LiDAR dataset were obtained.

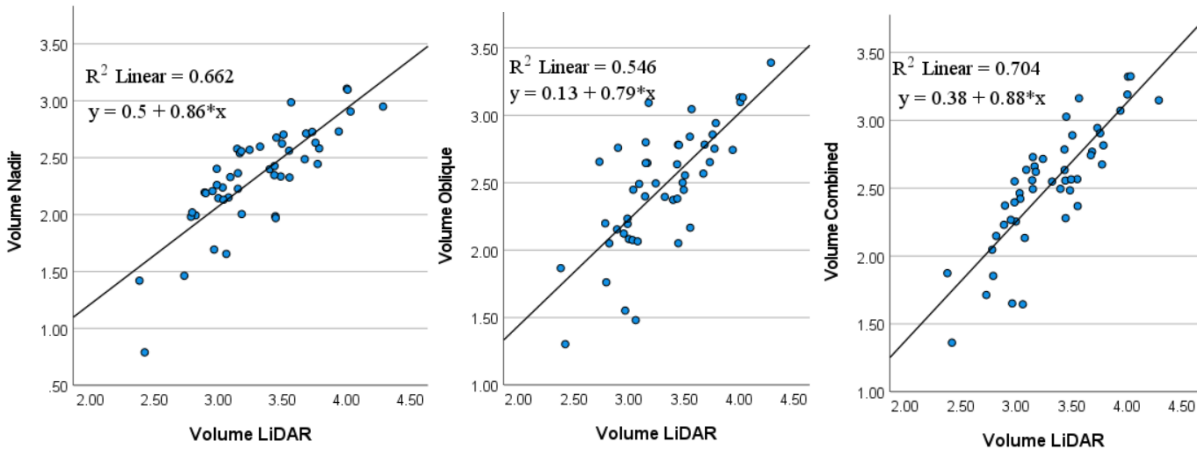

Figure 19. Linear regression between point cloud volumes of each flight and LiDAR point cloud volume.

The volume calculations display a relatively strong model fit for the nadir dataset with an R^2 of 0.66, and especially for the combined dataset with an R^2 of 0.70. However, the oblique flight by itself shows the lowest correlation with LiDAR volume with an R^2 of 0.55.

Regarding the heights and volumes of the point clouds, they are quite similar, except for the LiDAR point cloud, which displays notably higher values. Despite applying the same classification and segmentation methodology, the average height of the LiDAR point cloud exceeds that of the other datasets by more than 20 centimeters. Consequently, to improve the model fit, the LiDAR point cloud was further segmented by excluding the bottom 20 centimeters. This adjustment resulted in the following outcomes.

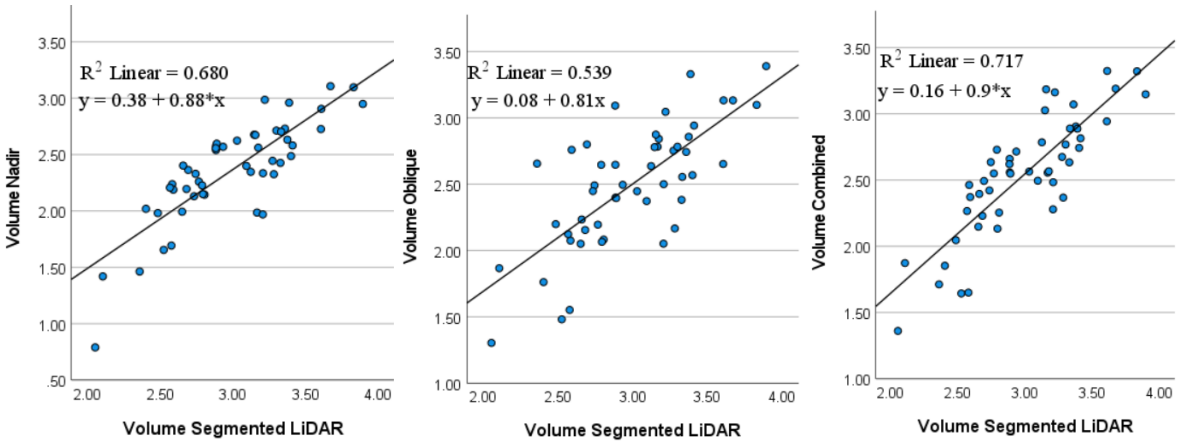

Figure 20. Linear regression between point cloud volumes of each flight and the volumes of the segmented LiDAR point cloud.

The R^2 values for the nadir and combined flights indicate an improvement of 0.02 and 0.01, respectively. However, there is a slight decrease of 0.01 in the R^2 value for the oblique point cloud. **Figure 20** illustrates that the combined datasets yield the most accurate volume calculation, making it the most suitable approach for generating a point cloud that closely represents the actual vineyard. The nadir flight demonstrates a similar level of accuracy, while the oblique flight, when considered alone, proves to be the least accurate.

While these volume calculations do not directly reflect the accuracy of the CWSI calculation, they do highlight that the nadir flight is more likely to generate a high-quality point cloud compared to the oblique flight. Moreover, combining both nadir and oblique flights ensures the best results in terms of point cloud accuracy.

5. Discussion

The objective of this study was to investigate the potential of using thermal point clouds within precision viticulture to assess water stress. To achieve this objective, 3D point clouds with Crop Water Stress Index (CWSI) values and 2D CWSI orthomosaics were created, and the differences between these data models were analyzed. The study also examined the impact of flight configuration on the CWSI calculation using point clouds. In this discussion the following points will be treated: address the research questions, interpret the results, discuss the limitations, and provide recommendations for future research.

5.1 Research questions and results

Research Question 1 (RQ1) aimed to understand the current state of water stress studies using multispectral and thermal UAV imagery data. The use of remote sensing data, including multispectral and thermal UAV imagery, has been widely explored in water stress assessment in various crops, including viticulture. These studies have demonstrated the potential of using these technologies to monitor and manage water stress in vineyards. This study contributes to this body of knowledge by specifically focusing on the use of thermal point clouds for CWSI analysis, which can offer a more comprehensive representation of the canopy compared to traditional 2D orthomosaics.

RQ2 addressed the methods of creating CWSI orthomosaics and point clouds using thermal UAV data. The results demonstrated successful generation and analysis of CWSI orthomosaics and point clouds using ArcGIS Pro, CloudCompare, Metashape and Python. The CHM provides a straightforward way to separate the soil from the canopy for both the orthomosaics and the point clouds. However, the maximum temperature values, approximately 55 °C for the nadir and combined flights, and 44 °C for the oblique flight, are higher than expected. Bian et al. (2017), utilizing the simplified CWSI approach, recorded a maximum cotton canopy of around 40 °C while the air temperature was 37 °C, which was higher than during the nadir flight. Consequently, their T_{dry} was considerably lower compared to the findings presented here. Similarly, Araújo-Paredes et al. (2022) reported lower temperature and T_{dry} values using the simplified CWSI method in a vineyard. These results strongly suggest that some soil or other noise pixels/points were inadvertently included instead of canopy only. Although the average temperature and generated maps indicate that these values mostly represent outliers, their presence had an impact on the CWSI calculation due to the histogram approach employed.

The orthomosaics provided valuable information about temperature and CWSI distribution over the vineyard, particularly in the top of the canopy. On the other hand, the point clouds offered a more detailed representation of the canopy, allowing for analysis of the side and bottom regions. Based on the findings presented in **Figure 15**, a consistent pattern emerges, revealing lower CWSI values at the top of the canopy, which progressively increase towards the bottom. This trend can be attributed to the influence of soil heat emission. Soil has a higher reflectance rate than plants in the thermal spectrum (Santesteban et al., 2017), which can be seen in **Figure 10**. Consequently, it is likely that the heat of the soil is transferred to the lower regions of the canopy, potentially contributing to the observed upward trend in CWSI values. This additional information provided by the point clouds can enhance the accuracy of water stress assessment by considering the entire canopy structure.

RQ3 and RQ4 aimed to explore the differences between the data models and the impact of flight angle on the CWSI calculation. The point clouds generated from the nadir and combined flights exhibited wider ranges of temperature and CWSI values compared to the orthomosaics. These differences can be attributed to the additional information captured by the point clouds, specifically from the side and bottom regions of the canopy. It is reasonable to expect that the minimum and maximum temperatures would exceed those of the orthomosaic since the point cloud captures more comprehensive data.

However, the oblique flight did not follow this pattern, showing a maximum temperature of 44.81 for the orthomosaic and 43.21 for the point cloud. One possible explanation for this inconsistency is a slight misalignment between the CHM and the temperature orthomosaic. As suggested by Zhou et al. (2021), misalignments in image co-registration can lead to the inclusion of soil pixels, which may account for the higher temperature values in the orthomosaic compared to the point cloud.

The linear regression analysis indicated a moderate correlation between the values obtained from the orthomosaic and the point cloud, suggesting that the point clouds provide additional insights beyond what can be obtained from the orthomosaics alone. To further investigate this, the regression analysis was repeated, this time with the top of the point cloud segmented. The R2 values for each flight increased: the nadir flight from 0.44 to 0.55, the oblique flight from 0.34 to 0.44, and the combined flight from 0.55 to 0.60. These increases highlight that part of

the differences between the point clouds and orthomosaics can be attributed to the additional information captured by the point clouds regarding the side and bottom of the canopy. This analysis suggests that point clouds offer advantages by considering the entire canopy structure.

However, since the correlation between the orthomosaics and point clouds was still only moderate, it is important to note that factors other than the side and bottom regions of the point cloud contribute to the differences between the data models. As previously discussed, the inclusion of soil pixels in the orthomosaic and potential errors in the classification and segmentation of the point cloud could have influenced the results. While the ground point classification function of Metashape is a reliable tool, some over or underestimation is still possible, resulting in the inclusion of soil points or the exclusion of canopy points. Additionally, distinguishing between trunks and the canopy proved challenging in the point cloud analysis due to the limitations of the UAV-based data acquisition and medium-quality point clouds used in this study.

Another regression analysis was performed to examine the relationship between CWSI values of different flights instead of different data models. The results indicated low R2 values between the nadir and oblique flights for both the point cloud and orthomosaic datasets, suggesting significant differences in CWSI between these flights. One possible explanation for this difference is the variation in temperature during the flight, resulting in the nadir flight recording higher temperatures compared to the oblique flight. Previous research by Agam et al. (2013) has shown that sunlight exposure can increase CWSI values in stressed trees by up to 0.3 within an hour, indicating that temperature differences can contribute significantly to the observed disparities in CWSI. Additionally, it is possible that the differences between the nadir and oblique flights are also influenced by the fact that both flights capture different parts of the canopy. However, if this were the case, it would be expected to have a greater impact on the point clouds rather than the orthomosaic. The results exhibited the opposite pattern, indicating that rather temperature difference than canopy coverage contributed to the observed differences.

Furthermore, an interesting finding from this regression analysis is that the point cloud exhibited similar regression coefficients between the nadir and combined flights (0.66) and between the oblique and combined flights (0.64). In contrast, the orthomosaic datasets showed higher regression coefficients for the nadir flights (0.93) compared to the oblique flights (0.12).

These findings highlight the added value of including both nadir and oblique angles in the point cloud analysis, as it combines information from both flights more evenly. In contrast, for the orthomosaic datasets, the nadir angle contributes significantly more than the oblique angle. This emphasizes the importance of considering flight configurations and angles when analyzing CWSI using 3D thermal point clouds instead of 2D orthomosaics.

The combination of nadir and oblique flights also demonstrated its added value in the volume analysis. When comparing point clouds to the LiDAR point cloud, which served as the ground-truth data, the combined flights exhibited the highest R^2 value (0.72), surpassing the nadir flight (0.68) and the oblique flight (0.54). This regression analysis highlights that the nadir flight is superior to the oblique flight in generating accurate point clouds, and the combination of both flights yields the best results.

These findings align partly with the research conducted by Lin et al. (2021), who investigated the impact of different flight angles on LAI estimation using point clouds. They observed that a combination of nadir and oblique flights consistently yielded the best results. However, their study also indicated that the oblique flight alone outperformed the nadir flight alone due to its coverage of the lower part of the canopy which differs from the current research. One explanation for this difference is that after segmenting the bottom of the LiDAR point cloud, the R^2 of the oblique point cloud slightly decreased, while the R^2 values for the other two flights increased. This discrepancy suggests that segmenting the bottom of the LiDAR point cloud may have diminished the contribution of the oblique flight, which captures the bottom of the canopy more effectively. The lower overall lower R^2 value of the oblique point cloud could be attributed to its lower quality, represented by a smaller point count (181,372 points compared to 215,199 points in the nadir point cloud). Although the convex hull method provided accurate results in estimating biomass using point clouds, Sangjan et al. (2022) showed that it can lead to volume overestimation in the presence of gaps within the point cloud.

5.2 Limitations and recommendations

Overall, the results of this study indicate the potential of using thermal point clouds for assessing water stress in precision viticulture. The point clouds offer a more detailed representation of the canopy structure, capturing information from the side and bottom regions

that are not captured by traditional 2D orthomosaics. This additional information can enhance the accuracy of water stress assessment and provide valuable insights into the overall water stress patterns within a vineyard. The findings of this study contribute to the existing literature on water stress assessment in viticulture and provide a foundation for further research in this field.

However, it is important to acknowledge the limitations of this study. Many crop stress analysis studies rely on ground-truth data obtained through direct plant measurements, such as leaf water potential or stomatal conductance (García-Tejero et al., 2018). Unfortunately, due to the high cost associated with acquiring the necessary instruments, such ground-truth data was not available for this study. As a result, the exact accuracy of both the orthomosaics and the point clouds cannot be definitively determined. While the use of temperature histograms for CWSI calculation and the CHM model for canopy extraction are valid methods, it is important to recognize that errors can still occur. This study attempted to mitigate these limitations by performing regression analysis and incorporating the LiDAR point cloud, which served as a reference data source. However, it is essential to note that without direct ground-truth measurements, the assessment of the absolute accuracy of the orthomosaics and point clouds remains uncertain. Future research could address these limitations by incorporating ground-truth data. By including direct plant measurements, it would be easier to determine the accuracy of the different methods and flights. This would help identify any shortcomings in the point cloud methodology and contribute to ongoing efforts to improve the methodology.

Furthermore, another important note is that the nadir flight was conducted during a significantly warmer period compared to the oblique flight, resulting in higher canopy temperatures and subsequently leading to different CWSI values. This temperature discrepancy introduces additional complexity when attempting to draw meaningful comparisons between the two flights. If the flights had been conducted simultaneously, any differences in CWSI values could be solely attributed to the influence of the flight angle, as both flights have undergone the same processing. However, the variations in CWSI values between the two flights demonstrated that when combining the flights, the orthomosaic predominantly incorporates values from the nadir flight, whereas the point cloud achieves a more balanced representation. Nevertheless, it is recommended that future research endeavours focus on conducting flights at the same time to mitigate the confounding influence of temperature

variations. By ensuring simultaneous data collection, other factors can be minimized, allowing for a more accurate assessment of the specific impact of the flight angle on CWSI calculations.

Finally, as previously discussed, the maximum temperature values strongly indicate that the analysis included not just canopy pixels and points, but also incorporated soil components. This suggests that the CHM utilized in the study did not perfectly separate soil from the canopy, leading to an influence on the accuracy of the CWSI calculation and subsequent analysis. To overcome this issue, excluding these outlier temperatures from the analysis would be preferable. However, establishing a clear threshold for identifying and removing such points and pixels becomes challenging and prone to arbitrary decisions if done manually.

In order to ensure equal processing of both point clouds and orthomosaics, the values were retained as they were. While the use of edge detection algorithms, such as the Canny edge algorithm, has shown promise in addressing these issues in CWSI applications (Araújo-Paredes et al., 2022), their application to point clouds remains a complex undertaking and is still in the beginning stages of research (Wu et al., 2023). Given the requirement for consistent processing of point clouds and orthomosaics to optimize comparative analysis, the CHM was chosen as the approach in this research.

Future research could benefit from exploring the integration of such algorithms into point cloud based CWSI analysis to enhance segmentation between soil and canopy. By utilizing advanced edge detection techniques, the accuracy and reliability of separating these components in point cloud data could be optimized, leading to more robust and accurate analysis results.

6. Conclusion

This study aimed to explore the potential of utilizing thermal point clouds in precision viticulture for water stress assessment. By generating 3D point clouds with CWSI values and comparing them with 2D CWSI orthomosaics, valuable insights into the differences and advantages of these data models were gained. Additionally, the impact of flight configuration on CWSI calculation using point clouds was assessed.

RQ 1 demonstrated that remote sensing data, including multispectral and thermal UAV imagery, have been extensively explored for water stress assessment in various crops, including viticulture. This study contributes by bridging the knowledge gap of the use of thermal point clouds within viticulture.

RQ2 addressed the methods of creating CWSI orthomosaics and point clouds using thermal UAV data. The CHM emerged as a useful tool for extracting canopy information and generating CWSI orthomosaics and point clouds. However, the results indicate that the model did not produce perfect outcomes and could benefit from optimization. Nevertheless, for the purpose of the exploratory analysis conducted in this research, the method proved to be sufficient. Utilizing point clouds allowed for analysis of the side and bottom regions, revealing a pattern of lower CWSI values at the top of the canopy, increasing towards the bottom. Such trends cannot be observed using orthomosaics, emphasizing the potential advantage offered by point clouds.

RQ 3 and 4 aimed to further understand the differences between data models and assess the impact of flight angles on CWSI calculations. The point clouds exhibited wider temperature and CWSI value ranges compared, suggesting that the additional information captured from the side and bottom regions of the canopy contributed to these differences. The linear regression analysis revealed a moderate correlation between orthomosaic and point cloud values, indicating that point clouds provide additional insights beyond the orthomosaics alone. Segmenting the top of the point cloud improved the correlation, emphasizing the advantages of point clouds in considering the entire canopy structure. However, the low R^2 values after segmentation indicate that the differences between the data models cannot be solely attributed to the inclusion of the side and bottom of the canopy in the point clouds. As a result, it is challenging to draw definitive conclusions about the accuracy of the CWSI point cloud.

The volume calculations demonstrated that the combination of nadir and oblique flights yielded the most accurate results, followed by the nadir flight alone, while the oblique flight showed the weakest performance. Although these findings do not directly pertain to the CWSI calculation, they suggest that capturing the canopy structure of the vineyard using a combination of nadir and oblique flights is likely to lead to more accurate CWSI assessments as well.

Based on these findings, this study demonstrates that thermal point clouds have the potential to assess water stress in precision viticulture. They provide a more comprehensive representation of the canopy and offer valuable insights into temperature and CWSI distribution throughout the vineyard. The combination of nadir and oblique flights in point cloud analysis yields the most accurate canopy representation. However, further research is needed to address the identified limitations and optimize the methodologies for practical implementation in vineyard management.

7. References

Agam, N., Cohen, Y., Alchanatis, V., & Ben-Gal, A. (2013). How sensitive is the CWSI to changes in solar radiation?. *International journal of remote sensing*, *34*(17), 6109-6120. DOI: https://doi.org/10.1080/01431161.2013.793873

Araújo-Paredes, C., Portela, F., Mendes, S., & Valín, M. I. (2022). Using Aerial Thermal Imagery to Evaluate Water Status in Vitis vinifera cv. Loureiro. *Sensors*, *22*(20), 8056. DOI: https://doi.org/10.3390/s22208056

Baíllo, A., & Chacón, J. E. (2021). Statistical outline of animal home ranges: an application of set estimation. In *Handbook of Statistics* (Vol. 44, pp. 3-37). Elsevier. DOI: https://doi.org/10.1016/bs.host.2020.10.002

Bello, S. A., Yu, S., Wang, C., Adam, J. M., & Li, J. (2020). Deep learning on 3D point clouds. *Remote Sensing*, *12*(11), 172. DOI: https://doi.org/10.3390/rs12111729

Bian, J., Zhang, Z., Chen, J., Chen, H., Cui, C., Li, X., ... & Fu, Q. (2019). Simplified evaluation of cotton water stress using high resolution unmanned aerial vehicle thermal imagery. *Remote Sensing*, *11*(3), 267. DOI: https://doi.org/10.3390/rs11030267

Bahat, I., Netzer, Y., Grünzweig, J. M., Alchanatis, V., Peeters, A., Goldshtein, E., Ohana-Levi, N., Ben-Gal, A. & Cohen, Y. (2021). In-season interactions between vine vigor, water status and wine quality in terrain-based management-zones in a 'Cabernet Sauvignon'vineyard. *Remote Sensing*, *13*(9), 1636. DOI: https://doi.org/10.3390/rs13091636

Buckley, T. N. (2019). How do stomata respond to water status?. *New Phytologist*, *224*(1), 21-36. DOI: https://doi.org/10.1111/nph.15899

Calderón, R., Navas-Cortés, J. A., Lucena, C., & Zarco-Tejada, P. J. (2013). High-resolution airborne hyperspectral and thermal imagery for early detection of Verticillium wilt of olive using fluorescence, temperature and narrow-band spectral indices. *Remote Sensing of Environment*, *139*, 231-245. DOI: https://doi.org/10.1016/j.rse.2013.07.031

Campos, J., García-Ruíz, F., & Gil, E. (2021). Assessment of vineyard canopy characteristics from vigour maps obtained using uav and satellite imagery. *Sensors*, *21*(7), 2363. DOI: https://doi.org/10.3390/s21072363

Cinat, P., Di Gennaro, S. F., Berton, A., & Matese, A. (2019). Comparison of unsupervised algorithms for Vineyard Canopy segmentation from UAV multispectral images. *Remote Sensing*, *11*(9), 1023. DOI: https://doi.org/10.3390/rs11091023

Cohen, Y., Alchanatis, V., Meron, M., Saranga, Y., & Tsipris, J. (2005). Estimation of leaf water potential by thermal imagery and spatial analysis. *Journal of experimental botany*, *56*(417), 1843-1852. DOI: https://doi.org/10.1093/jxb/eri174

Comba, L., Biglia, A., Aimonino, D. R., Barge, P., Tortia, C., & Gay, P. (2019, October). 2D and 3D data fusion for crop monitoring in precision agriculture. In *2019 IEEE International Workshop on Metrology for Agriculture and Forestry (MetroAgriFor)* (pp.62-67).IEEE. DOI: https://doi.org/10.1109/MetroAgriFor.2019.8909219

Drew, P. L., Sudduth, K. A., Sadler, E. J., & Thompson, A. L. (2019). Development of a multi-band sensor for crop temperature measurement. *Computers and Electronics in Agriculture*, *162*, 269-280. DOI: https://doi.org/10.1016/j.compag.2019.04.007

Egea, G., Padilla-Díaz, C. M., Martinez-Guanter, J., Fernández, J. E., & Pérez-Ruiz, M. (2017). Assessing a crop water stress index derived from aerial thermal imaging and infrared thermometry in super-high density olive orchards. *Agricultural Water Management*, *187*, 210-221. DOI: https://doi.org/10.1016/j.agwat.2017.03.030

Feng, A., Zhou, J., Vories, E. D., Sudduth, K. A., & Zhang, M. (2020). Yield estimation in cotton using UAV-based multi-sensor imagery. *Biosystems Engineering*, *193*, 101-114. DOI: https://doi.org/10.1016/j.biosystemseng.2020.02.014

Fuentes, S., De Bei, R., Pech, J., & Tyerman, S. (2012). Computational water stress indices obtained from thermal image analysis of grapevine canopies. *Irrigation Science*, *30*(6), 523-536.

Gates, D. M. (1964). Leaf temperature and transpiration 1. *Agronomy Journal*, *56*(3), 273-277. DOI: https://doi.org/10.2134/agronj1964.00021962005600030007x

García-Tejero, I. F., Rubio, A. E., Viñuela, I., Hernández, A., Gutiérrez-Gordillo, S., Rodríguez-Pleguezuelo, C. R., & Durán-Zuazo, V. H. (2018). Thermal imaging at plant level to assess the crop-water status in almond trees (cv. Guara) under deficit irrigation strategies. *Agricultural water management*, *208*, 176-186. DOI: https://doi.org/10.1016/j.agwat.2018.06.002

González, O., Lizarraga, M. I., Karaman, S., & Salas, J. (2019). Thermal Radiation Dynamics of Soil Surfaces with Unmanned Aerial Systems. In *Pattern Recognition: 11th Mexican Conference, MCPR 2019, Querétaro, Mexico, June 26–29, 2019, Proceedings 11* (pp. 183-192). Springer International Publishing.

Grechi, G., Fiorucci, M., Marmoni, G. M., & Martino, S. (2021). 3D thermal monitoring of jointed rock masses through infrared thermography and photogrammetry. *Remote Sensing*, *13*(5), 957. DOI: https://doi.org/10.3390/rs13050957

Guilbert, V., Antoine, R., Heinkele, C., Maquaire, O., Costa, S., Gout, C., Davidson, R., Sorin, J., Beaucamp, B. & Fauchard, C. (2020). Fusion of thermal and visible point clouds: Application to the Vaches Noires landslide, Normandy, France. *ISPRS-International Archives of the Photogrammetry, Remote Sensing and Spatial Information Sciences*, *43*, 227-232.

Gutiérrez, S., Diago, M. P., Fernández-Novales, J., & Tardaguila, J. (2018). Vineyard water status assessment using on-the-go thermal imaging and machine learning. *PLoS One*, *13*(2), e0192037. DOI: https://doi.org/10.1371/journal.pone.0192037

Idso, S. B., Jackson, R. D., Pinter Jr, P. J., Reginato, R. J., & Hatfield, J. L. (1981). Normalizing the stress-degree-day parameter for environmental variability. *Agricultural meteorology*, *24*, 45-55. DOI: https://doi.org/10.1016/0002-1571(81)90032-7

Irmak, S., Haman, D. Z., & Bastug, R. (2000). Determination of crop water stress index for irrigation timing and yield estimation of corn. *Agronomy Journal*, *92*(6), 1221-1227. DOI: https://doi.org/10.2134/agronj2000.9261221x

Jackson, R. D., Idso, S. B., Reginato, R. J., & Pinter Jr, P. J. (1981). Canopy temperature as a crop water stress indicator. *Water resources research*, *17*(4), 1133-1138. DOI: https://doi.org/10.1029/WR017i004p01133

Jones, H. G. (1999). Use of infrared thermometry for estimation of stomatal conductance as a possible aid to irrigation scheduling. *Agricultural and forest meteorology*, *95*(3), 139-149. DOI: https://doi.org/10.1016/S0168-1923(99)00030-1

Jones, H. G., Stoll, M., Santos, T., Sousa, C. D., Chaves, M. M., & Grant, O. M. (2002). Use of infrared thermography for monitoring stomatal closure in the field: application to grapevine. *Journal of experimental botany*, *53*(378), 2249-2260. DOI: https://doi.org/10.1093/jxb/erf083

Jurado, J. M., López, A., Pádua, L., & Sousa, J. J. (2022). Remote sensing image fusion on 3D scenarios: A review of applications for agriculture and forestry. *International Journal of Applied Earth Observation and Geoinformation*, *112*, 102856. DOI: https://doi.org/10.1016/j.jag.2022.102856

Khanal, S., Fulton, J., & Shearer, S. (2017). An overview of current and potential applications of thermal remote sensing in precision agriculture. *Computers and Electronics in Agriculture*, *139*, 22-32. DOI: https://doi.org/10.1016/j.compag.2017.05.001

Koenig, K., Höfle, B., Hämmerle, M., Jarmer, T., Siegmann, B., & Lilienthal, H. (2015). Comparative classification analysis of post-harvest growth detection from terrestrial LiDAR point clouds in precision agriculture. *ISPRS Journal of Photogrammetry and Remote Sensing*, *104*, 112-125. DOI: https://doi.org/10.1016/j.isprsjprs.2015.03.003

Li, M., Shamshiri, R. R., Schirrmann, M., Weltzien, C., Shafian, S., & Laursen, M. S. (2022). UAV oblique imagery with an adaptive micro-terrain model for estimation of leaf area index and height of maize canopy from 3D point clouds. *Remote Sensing*, *14*(3), 585. DOI: https://doi.org/10.3390/rs14030585

Liao, J., Zhou, J., & Yang, W. (2021). Comparing LiDAR and SfM digital surface models for three land cover types. *Open Geosciences*, *13*(1), 497-504. DOI: https://doi.org/10.1515/geo-2020-0257

Lin, L., Yu, K., Yao, X., Deng, Y., Hao, Z., Chen, Y., ... & Liu, J. (2021). UAV based estimation of forest leaf area index (LAI) through oblique photogrammetry. *Remote Sensing*, *13*(4), 803. DOI: https://doi.org/10.3390/rs13040803

Mack, J., Lenz, C., Teutrine, J., & Steinhage, V. (2017). High-precision 3D detection and reconstruction of grapes from laser range data for efficient phenotyping based on supervised learning. *Computers and Electronics in Agriculture*, *135*, 300-311. DOI: https://doi.org/10.1016/j.compag.2017.02.017

Matese, A., & Di Gennaro, S. F. (2015). Technology in precision viticulture: A state of the art review. *International journal of wine research*, *7*, 69-81.

Meddens, A. J., Vierling, L. A., Eitel, J. U., Jennewein, J. S., White, J. C., & Wulder, M. A. (2018). Developing 5 m resolution canopy height and digital terrain models from WorldView and ArcticDEM data. *Remote Sensing of Environment*, *218*, 174-188. DOI: https://doi.org/10.1016/j.rse.2018.09.010

Meron, M., Tsipris, J., Orlov, V., Alchanatis, V., & Cohen, Y. (2010). Crop water stress mapping for site-specific irrigation by thermal imagery and artificial reference surfaces. *Precision agriculture*, *11*(2), 148-162.

Messina, G., & Modica, G. (2020). Applications of UAV thermal imagery in precision agriculture: State of the art and future research outlook. *Remote Sensing*, *12*(9), 1491. DOI: https://doi.org/10.3390/rs12091491

MicaSense. (2022, September 01). *Altum-PT Integration guide*. https://support.micasense.com/hc/en-us/articles/4419868608407-Altum-PT-Integration-Guide

Myneni, R. B., Hall, F. G., Sellers, P. J., & Marshak, A. L. (1995). The interpretation of spectral vegetation indexes. *IEEE Transactions on Geoscience and remote Sensing*, *33*(2), 481-486. DOI: https://doi.org/10.1109/TGRS.1995.8746029

Narvaez, F. Y., Reina, G., Torres-Torriti, M., Kantor, G., & Cheein, F. A. (2017). A survey of ranging and imaging techniques for precision agriculture phenotyping. *IEEE/ASME Transactions on Mechatronics*, *22*(6), 2428-2439. DOI: https://doi.org/10.1109/TMECH.2017.2760866

Neinavaz, E., Schlerf, M., Darvishzadeh, R., Gerhards, M., & Skidmore, A. K. (2021). Thermal infrared remote sensing of vegetation: Current status and perspectives. *International Journal of Applied Earth Observation and Geoinformation*, *102*, 102415. DOI: https://doi.org/10.1016/j.jag.2021.102415

Padhi, J., Misra, R. K., & Payero, J. (2009). Use of infrared thermography to detect water deficit response in an irrigated cotton crop. *Water Resources and Watershed Management (WRWM)*, 1-10.

Pagliai, A., Ammoniaci, M., Sarri, D., Lisci, R., Perria, R., Vieri, M., ... & Kartsiotis, S. P. (2022). Comparison of Aerial and Ground 3D Point Clouds for Canopy Size Assessment in Precision Viticulture. *Remote Sensing*, *14*(5), 1145. DOI: https://doi.org/10.3390/rs14051145

Parkash, V., & Singh, S. (2020). A review on potential plant-based water stress indicators for vegetable crops. *Sustainability*, *12*(10), 3945. DOI: https://doi.org/10.3390/su12103945

Park, S., Ryu, D., Fuentes, S., Chung, H., Hernández-Montes, E., & O'Connell, M. (2017). Adaptive estimation of crop water stress in nectarine and peach orchards using high-resolution imagery from an unmanned aerial vehicle (UAV). *Remote Sensing*, *9*(8), 828. DOI: https://doi.org/10.3390/rs9080828

Pendleton, S. D., Andersen, H., Du, X., Shen, X., Meghjani, M., Eng, Y. H., ... & Ang Jr, M. H. (2017). Perception, planning, control, and coordination for autonomous vehicles. *Machines*, *5*(1), 6. DOI: https://doi.org/10.3390/machines5010006

Poblete-Echeverría, C., Espinace, D., Sepúlveda-Reyes, D., Zúñiga, M., & Sanchez, M. (2015). Analysis of crop water stress index (CWSI) for estimating stem water potential in

grapevines: Comparison between natural reference and baseline approaches. In *VIII International Symposium on Irrigation of Horticultural Crops 1150* (pp. 189-194). DOI: https://doi.org/10.17660/ActaHortic.2017.1150.27

Poblete, T., Ortega-Farías, S., Moreno, M. A., & Bardeen, M. (2017). Artificial neural network to predict vine water status spatial variability using multispectral information obtained from an unmanned aerial vehicle (UAV). *Sensors*, *17*(11), 2488. DOI: https://doi.org/10.3390/s17112488

Prasad, S., Bruce, L. M., & Chanussot, J. (2011). Optical remote sensing. *Advances in Signal Processing and Exploitation Techniques; Springer: Berlin, Germany*.

Ramón, A., Adán, A., & Castilla, F. J. (2022). Thermal Point Clouds of Buildings: A review. *Energy and Buildings*, 112425. DOI: https://doi.org/10.1016/j.enbuild.2022.112425

Rouse J.W., Haas R.H., Schell J.A., Deering D.W. (1974). Monitoring vegetation systems in the Great Plains with ERTS. *Proceedings, 3rd Earth Resource Technology Satellite (ERTS*), Symposium 1, 48–62.

Rud, R., Cohen, Y., Alchanatis, V., Levi, A., Brikman, R., Shenderey, C., ... & Nigon, T. (2014). Crop water stress index derived from multi-year ground and aerial thermal images as an indicator of potato water status. *Precision Agriculture*, *15*(3), 273-289.

Sánchez-Piñero, M., Martín-Palomo, M.J., Andreu, L., Moriana, A., & Corell, M. (2022). Evaluation of a simplified methodology to estimate the CWSI in olive orchards. *Agricultural Water Management*, 269, 107729. DOI: https://doi.org/10.1016/j.agwat.2022.107729

Sangjan, W., McGee, R. J., & Sankaran, S. (2022). Optimization of UAV-based imaging and image processing orthomosaic and point cloud approaches for estimating biomass in a forage crop. *Remote Sensing*, *14*(10), 2396. DOI: https://doi.org/10.3390/rs14102396

Santesteban, L. G., Di Gennaro, S. F., Herrero-Langreo, A., Miranda, C., Royo, J. B., & Matese, A. (2017). High-resolution UAV-based thermal imaging to estimate the instantaneous and seasonal variability of plant water status within a vineyard. *Agricultural Water Management*, *183*, 49-59. DOI: https://doi.org/10.1016/j.agwat.2016.08.026

Sassu, A., Gambella, F., Ghiani, L., Mercenaro, L., Caria, M., & Pazzona, A. L. (2021). Advances in Unmanned Aerial System Remote Sensing for Precision Viticulture. *Sensors*, *21*(3), 956. DOI: https://doi.org/10.3390/s21030956

Schonberger, J. L., & Frahm, J. M. (2016). Structure-from-motion revisited. In *Proceedings of the IEEE conference on computer vision and pattern recognition* (pp. 4104-4113).

Stark, B., Smith, B., & Chen, Y. (2014). Survey of thermal infrared remote sensing for Unmanned Aerial Systems. In *2014 International Conference on Unmanned Aircraft Systems (ICUAS)* (pp. 1294-1299). IEEE. DOI: https://doi.org/10.1109/ICUAS.2014.6842387

Tabib, R. A., Jadhav, Y. V., Tegginkeri, S., Gani, K., Desai, C., Patil, U., & Mudenagudi, U. (2020). Learning-based hole detection in 3D point cloud towards hole filling. *Procedia Computer Science*, *171*, 475-482. DOI: https://doi.org/10.1016/j.procs.2020.04.050

Testi, L., Goldhamer, D. A., Iniesta, F., & Salinas, M. (2008). Crop water stress index is a sensitive water stress indicator in pistachio trees. *Irrigation science*, *26*(5), 395-405.

Torres-Sánchez, J., Mesas-Carrascosa, F. J., Santesteban, L. G., Jiménez-Brenes, F. M., Oneka, O., Villa-Llop, A., ... & López-Granados, F. (2021). Grape cluster detection using UAV photogrammetric point clouds as a low-cost tool for yield forecasting in vineyards. *Sensors*, *21*(9), 3083. DOI: https://doi.org/10.3390/s21093083

Vadivambal, R., & Jayas, D. S. (2011). Applications of thermal imaging in agriculture and food industry—a review. *Food and bioprocess technology*, *4*(2), 186-199.

Wallace, L., Lucieer, A., Malenovský, Z., Turner, D., & Vopěnka, P. (2016). Assessment of forest structure using two UAV techniques: A comparison of airborne laser scanning and structure from motion (SfM) point clouds. *Forests*, *7*(3), 62. DOI: https://doi.org/10.3390/f7030062

Walker, G. K., & Hatfield, J. L. (1983). Stress Measurement Using Foliage Temperatures 1. *Agronomy Journal*, *75*(4), 623-629. DOI: https://doi.org/10.2134/agronj1983.00021962007500040012x

Webster, C., Westoby, M., Rutter, N., & Jonas, T. (2018). Three-dimensional thermal characterization of forest canopies using UAV photogrammetry. *Remote Sensing of Environment*, *209*, 835-847. DOI: https://doi.org/10.1016/j.rse.2017.09.033

Weingarten, J. W., Gruener, G., & Siegwart, R. (2004, September). A state-of-the-art 3D sensor for robot navigation. In *2004 IEEE/RSJ International Conference on Intelligent Robots and Systems (IROS)(IEEE Cat. No. 04CH37566)* (Vol. 3, pp. 2155-2160). IEEE. DOI: https://doi.org/10.1109/IROS.2004.1389728

Weiss, M., & Baret, F. (2017). Using 3D point clouds derived from UAV RGB imagery to describe vineyard 3D macro-structure. *Remote Sensing*, *9*(2), 111. DOI: https://doi.org/10.3390/rs9020111

Wójtowicz, M., Wójtowicz, A., & Piekarczyk, J. (2016). Application of remote sensing methods in agriculture. *Communications in Biometry and Crop Science*, *11*(1), 31-50.

Xie, Y., Tian, J., & Zhu, X. X. (2020). Linking points with labels in 3D: A review of point cloud semantic segmentation. *IEEE Geoscience and remote sensing magazine*, *8*(4), 38-59. DOI: https://doi.org/10.1109/MGRS.2019.2937630

Zhang, C., & Kovacs, J. M. (2012). The application of small unmanned aerial systems for precision agriculture: a review. *Precision agriculture*, *13*(6), 693-712.

Zhang, J., Tian, H., Wang, D., Li, H., & Mouazen, A. M. (2021). A novel spectral index for estimation of relative chlorophyll content of sugar beet. *Computers and Electronics in Agriculture*, *184*, 106088. DOI: https://doi.org/10.1016/j.compag.2021.106088

Zhou, Z., Majeed, Y., Naranjo, G. D., & Gambacorta, E. M. (2021). Assessment for crop water stress with infrared thermal imagery in precision agriculture: A review and future prospects for deep learning applications. *Computers and Electronics in Agriculture*, *182*, 106019. DOI: https://doi.org/10.1016/j.compag.2021.106019